UC-25
LBL-6278
c. 1

PRECIPITATION-STRENGTHENED AUSTENITIC FE-MN-TI ALLOYS

Keh-Minn Chang
M. S. thesis

June 1977

Prepared for the U. S. Energy Research and Development Administration under Contract W-7405-ENG-48

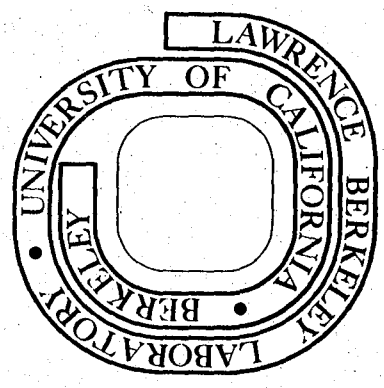

LBL-6278
c. 1

PRECIPITATION-STRENGTHENED AUSTENITIC Fe-Mn-Ti ALLOYS

Keh-Minn Chang
Department of Materials Science and Mining Engineering
Materials and Molecular Research Division, Lawrence Berkeley Laboratory
University of Califonia, Berkeley, California 94720

ABSTRACT

The precipitation of the intermetallic compounds in the Fe-20Mn-2Ti and Fe-28Mn-2Ti alloy systems has been investigated over the temperature range 700°C to 900°C using hardness measurements, optical and scanning electron microscopy, and X-ray diffraction. In both systems only the equilibrium Laves phase was found to form during the ausaging process; no transition phase was observed. The precitate was identified as a C14 ($MgZn_2$) type hexagonal Laves phase with a chemical composition close to $Fe_2(Ti,Mn)$. The precipitation in an as-solution-treated sample occurred predominantly in a heterogeneous manner, predominantly along grain boundaries.

The alloys were cold rolled between the solution annealing and aging processes. In addition to the high density of dislocations, martenisitic phases were induced by deformation; a $\gamma \rightarrow \varepsilon$ transformation occurred in the Fe-28Mn-2Ti alloy while a $\gamma \rightarrow \alpha'$ transformation was predominant in the Fe-20Mn-2Ti alloy. Subsequent ausaging was conducted at the temperature above A_f, which resulted in the matrices maintaining the austenitic form after cooling to room temperature. With sufficient nucleation sites, a large number of very fine precipitates formed randomly in the matrices within a short aging period. This aging treatment resulted in a increase in yield strength. The enchancement of mechanical properties is due to the randomly distributed precipitates combined with the high

PRECIPITATION-STRENGTHENED AUSTENITIC Fe-Mn-Ti ALLOYS

Contents

PRECIPITATION-STRENGTHENED AUSTENITIC Fe-Mn-Ti ALLOYS

Master of Science of Engineering | Keh-Minn Chang | Physical Metallurgy

Chairman of Committee

ABSTRACT

The precipitation of the intermetallic compounds in the Fe-20Mn-2Ti and Fe-28Mn-2Ti alloy systems has been investigated over the temperature range 700°C to 900°C using hardness measurements, optical and scanning electron microscopy, and x-ray diffraction. In both systems only the equilbrium Laves phase was found to form during the ausaging process; no transition phase was observed. The precipitate was identified as a C14 ($MgZn_2$) type hexagonal Laves phase with a chemical composition close to $Fe_2(Ti,Mn)$. The precipitation in an as-solution-treated sample occurred predominantly in a heterogeneous manner, predominantly along grain boundaries.

The alloys were cold rolled between the solution annealing and aging processes. In addition to the high density of dislocations, martenisitc phases were induced by deformation; a $\gamma \rightarrow \varepsilon$ transformation occurred in the Fe-28Mn-2Ti alloy while a $\gamma \rightarrow \alpha'$ transformation was predominant in the Fe-20Mn-2Ti alloy. Subsequent ausaging was conducted at the temperature above A_f, which resulted in the matrices maintaining the austenitic form after cooling to room temperature. With sufficient nucleation sites, a large number of very fine precipitates formed randomly in the matrices within a short aging period. This aging treatment resulted in a increase in yield strength. The enhancement of mechanical properties is due to the randomly distributed precipitates combined with the high

defect density and find substructure. Approximately 20% uniform elongation was observed in the tensile tests. This ductility results from a strain-induced transformation.

I. INTRODUCTION

Austenitic iron-base alloys containing high manganese content have been developed and commercially used for various purposes. The austenitic structure of these alloys is mechanically unstable unless a large amount of manganese or other austenite stabilizer is added. [1] The metastable parent phase undergoes a martensitic phase transformation when it is subjected to deformation at temperature lower than M_d. To benificially utilize this phenomenum, the thermomechanical treatment used in "TRIP" (transformation induced plasticity) steels [2] has been applied to some of high manganese steels. [3,4] The mechanically induced transformation including γ (fcc) $\rightarrow$ ε (hcp) and γ (fcc) $\rightarrow$ α' (bcc) has been shown to improve the tensile strength and the ductility.

From an economic point of view, manganese is a very promising austenite stabilizing element for iron-base alloys. Substituting manganese for nickel in austenitic stainless steel, like AISI 200 Series, has been effectively utilized to reduce materials cost without sacrificing properties for more than twenty years. [5] Most of commercial high manganese steels contain interstitial hardening elements, such as carbon or nitrogen. [6,7] They contribute to the strength of the matrix by forming precipitates of carbides or nitrides. The difficulty in processing and the thermal instability of interstitial precipitates put a limit on their desirability in high manganese steels. Therefore, efforts are underway to use intermetallic compounds to strengthen high manganese, iron-based alloys.

The occurrence of intermetallic phases in iron has been summarized by Nevitt. [8] Table I is a general resumé of possible phases based on B elements such as manganese, iron, cobalt and nickel with additions of

A elements from the titanium, vanadium, chromium groups of the Periodic Table. Three factors: electron/atom ratio, atomic size, and compressibility, are important in determining alloy chemistry. The phases listed in Table 1 can be classified into two groups on the basis of the atomic arrangement within their crystal structures. In one group there are the geometrically close-packed phases which contain both octahedral and tetrahedral interstices e.g. B_3A. In the other group, there are the topologically close packed phase which contain only tetrahedral interstices, e.g. Laves (B_2A), σ, μ, and χ. Technically, B_3A is the most important intermetallic compound in austenitic iron alloys. This is due to its natural morphology with small interparticle distance, large volume percent, and preference for general precipitation. Further favorable factors are coherency with close lattice matching, and the high ductility of the phase compared with other precipitates.

Unfortunately, no such phase has been found with the B element being manganese or iron. The most likely phase to exist in Fe-Mn austenite is the B_2A Laves phase which as reported [9] embrittles alloys at room temperature but seems to have a strengthening effect at high temperatures. The embrittlement caused by Laves phases is attributed to the continuing precipitation along grain boundaries. By eliminating this continuous grain boundary precipitation, Laves phases can be effectively utilized to strengthen an iron matrix. Jin [10] was successful in spheroidization of the grain boundary Laves phase by cycling through the α -γ phase transformation. The fracture mode changed from inter-granular cleavage to the ductile rupture.

The objective of the present study was to investigate the precipitation behavior in the Fe-Mn austenites containing titanium as the hardening

element. Aging characteristics, precipitate distribution and identification, and mechanical property measurement were conducted on (1) completely austenitic and (2) ε-phase bearing austenitic Fe-Mn-Ti alloys. The Laves phases Fe_2Ti and Mn_2Ti have been observed in the binary phase diagram. [11] The existence of the compound Fe_2Mn in the Fe-Mn equilibrium diagram has been proposed by Soviet workers [12] though its existence is not commonly accepted. Determining the chemical composition of the precipitate which is thermodynamically favorable will help in further understanding the ternary phase diagram.

The Orowan [13] strengthening mechanism of second phase particles suggests that the strength of an alloy containing a dispersion of fine particles is determined by the spacing between particles. The precipitation of Laves phases cannot contribute much strengthening since, in most cases, these phases heterogeneously nucleate and grow continuously along grain boundaries. Intergranular fracture is likely to occur resulting in reduced ductility. If a large number of nucleation sites are introduced in the matrix before the aging process, however, rapid nucleation can take place and continuous grain boundary precipitation can be avoided. The kinetics of matrix precipitation is then much faster and separate fine precipitates with small spacings will form. This uniform matrix precipitation can be facilitated by the high denisty of dislocations generated by heavy deformation. [14] The stored strain energy of these defects will aid in the heterogeneous nucleation of Laves phases inside the matrix rather than along grain boundaries. For the mechanically unstable Fe-Mn austenite, the induced phase size is much smaller than the grain size; and hence, the interfaces between induced and parent phases will be effective nucleation sites for Laves phases.

Following deformation the aging process can be conducted at a temperature just above A_f, so that the matrix phase will revert to the austenitic structure. With a highly deformed structure isothermal aging requires less time and lower temperature since the precipitation kinetics is faster. If the cold work effect is not completely recovered, the TRIP mechanism may occur during subsequent deformation.

II. EXPERIMENTAL PROCEDURES

A. MATERIAL PREPARATION

Alloys were made using high purity (99.9%) iron, manganese, and titanium which were induction melted in magnesium oxide crucibles under an argon atmosphere. Ingots were cast in two copper chill molds: one is 10kg, 7 cm. dia.; the other is 4.5kg, 3 cm. dia. The nominal and actual compositions of the alloys used in the present study are given in Table II.

The ingots were homogenized at 1200°C for 24 hrs under a partial pressure of argon gas (~0.38 torr) and then furnace cooled. After being reheated to 1100°C, the 10kg ingots were upset and cross-forged to plates of thickness 1.3 cm. and 2.5 cm. while the 4.5kg ingots were simply forged to plates of 1.3 cm. thick. After forging, the plates were water quenched. Finally, the plates were sectioned to the dimensions required by specimens for different tests using a dimet saw with water cooling.

B. HEAT TREATMENT

Before each heat treatment, all specimens were carefully polished to remove the oxidation layer created by the previous heat treatment. The specimens were put into stainless steel bags, filled with argon gas, and then sealed. All alloys were solution treated at 1150°C for 1½ hours and ice-brine quenched. Resealed into steel bags separately, specimens were aged at 700°C, 800°C, and 900°C for different times and water quenched. To study the effects of cold work on precipitation, specimens were cold rolled 50% between the solution annealing and the aging process.

Each specimen was polished on emery paper to 0000 grit after heat treatment. Subsequent chemical polishing was carried out using dilute hydrofluoric acid solution (100ml H_2O_2 + 4mℓHF) to remove residual deformation

due to polishing.

C. MECHANICAL TESTS

1. Hardness Tests:

Hardness measurements were performed using a Wilson Rockwell Hardness Tester in the Rockwell "B" scale (100kg major load, 1/16 in. dia. steel ball) for the specimens which were simply aged. The predeformed and aged specimens were tested in the Rockwell "C" scale (150kg major load, diamond Braile indentor). Elapsed time 15 sec. was taken for all tests after applying the major load. At least five indentations were made for each hardness measurement, and the results were averaged and the standard deviations calculated.

2. Tensile Tests:

The tensile properties were determined on a 5,000kg capacity Instron Testing Machine at a crosshead speed 0.2cm/min. Flat tensile specimens of 2.54cm gauge length and 0.635cm x 0.3175cm cross section were employed. Tests were conducted at room temperature and two specimens were tested for each datum.

3. Charpy Impact Tests:

Impact tests were carried out on a 225 ft-lb capacity impact testing machine. For each heat treatment, two standard ASTME 23-72 Charpy V-notch specimens were tested. The tests were run at room temperature.

D. X-RAY DIFFRACTION

Quatitative x-ray analysis was carried out using a Picker x-ray diffractometer to verify the crystal structure of precipitates and matrices. A copper tube was employed to produce the CuK α radiation as the x-ray source, and a (200) LiF crystal mono-chrometer was placed between the diffracted beam and detector to eliminate the fluorescence background.

Relative volume fraction of phases in alloys were calculated by comparing the integrated intensities of the corresponding diffracted radiation. Volume ratio between γ and ε phase were obtained by examining (200)γ and (10.1)ε peaks, while (311)γ, (220)γ, and (211)α peaks were measured for estimating the volume ration of γ to α phase. The mathematical technique used is explained in detail by Cullity [11].

E. OPTICAL MICROSCOPY

Specimens which had been chemically polished were etched for optical microscopic observation using a 5% Nital etching solution (95ml C_2H_5OH + 5ml HNO_3). Schumann reagent (100ml cold saturated $Na_2S_2O_3$ + 5gm $K_2S_2O_5$) was applied whenever ε phase existed in a specimen since the reagent was reported [12] to be excellent in delineating the ε phase contrast.

F. SCANNING ELECTRON MICROSCOPY AND ENERGY DISPERSION ANALYSIS OF X-RAY

JEM-U3 scanning electron microscope (SEM) accompanied with an x-ray energy dispersive spectrometer was ultilized to identify the the precipitates. The block diagram of Energy Dispersive Analysis of x-ray (EDAX) is shown in Fig. 1. An electron beam of 200Å dia. was focused at the precipitate which had been exposed by overetching the specimen surface. The energy spectrum of the characteristic x-ray emitted from the precipitate was collected by a silicon crystal detector, and processed by computer. The preset program converted the data to the chemical composition of the precipitate.

Carbon replicas which extracted precipitates from the overetched surface of specimens were used for more accurate examination of chemical composition analysis by EDAX, since the involvement of matrix in creating characterisitic x-rays might cause some error. The specimen surface must

be prepared in a satisfactory manner for an accurate result. The accuracy of the composition analysis should be within 2%.

The fracture surfaces of broken tensile and Charpy specimens were examined with SEM operated at 20KV via secondary electron emission.

G. TRANSMISSION ELECTRON MICROSCOPY

Thin slices (0.05cm thick) were cut from the interior of bulk alloys and prepared for transmission electron microscopy. Following a chemical polish in the dilute hydrofluoric acid solution to 0.0075cm thick, the thin foil was spark-cut into 3.0mm diameter discs and jet-thinned using the solution of 75gm Cr_2O_3 + 400 ml CH_3COOH + 21ml H_2O.

The specimens were examined in a Hitachi HU -125 electron microscope operating at 100KV.

III. RESULTS AND DISCUSSIONS

A. PHASE RELATIONS

The volume fractions of different phases observed by x-ray diffraction analysis for different thermal treatments are listed in Table III. The crystal structure of the Fe-Mn system having 28 wt pt or greater Mn, becomes fully austenitic (γ) at room temperature. The hexagonal phase, ε, was not detected by the x-ray technique in an as-annealed Fe-28Mn alloy, but traces of ε phase were observed under the optical microscope (Fig. 2a). In the alloy with 20 wt pt Mn, increasing amounts of ε phase (up to about 70%) formed upon cooling from a solution annealing to room temperature. A typical microstructure of mixed γ and ε phases is shown in Fig. 3a. No body-centered cubic α' formed in both alloys even when cooled to liquid nitrogen temperature (-196^{o}C). These results are consistent with previous observations [12]. Some authors [16,17] attribute the formation of ε phase in Fe-Mn system to the effect of Mn on (1) the kinetics of austenite decomposition and (2) the stacking fault energy of the austenite. With increasing Mn content, not only is the transformation temperature lowered, but there is also a decrease in the austenitic stacking fault energy. The combined effects of increasing Mn is to accelerate the $\gamma \rightarrow \varepsilon$ transformation as the austenite stacking fault energy approaches zero.

With the addition of titanium in both systems, the amount of ε phase decreases dramatically and more γ pahse is retained at room temperature. In the as-annealed condition, a completly austenitic phase was observed in the Fe-28Mn-2Ti alloy (Fig. 2b). Less than 10% of ε phase formed in the Fe-20Mn-2Ti alloy (Fig. 3b). The influence of Ti on the $\gamma \rightarrow \varepsilon$ transformation is not well characterized. Previous workers [18] observed that titanium additions can reduce the austenitic stacking fault energy

of some Fe-Ni-Cr alloys. Yeo [19] and Abraham, et al [20] found that the M_s temperature of Fe-Ni-Ti systems decrease with increasing Ti content. Whether the stacking fault energy of the Fe-Mn austenite is lowered by titanium additions is still unknown. However, it is clear from present results that Ti decreases the M_s temperature of the Fe-Mn austenite; i.e. Ti is a strong austenite stabilizer for Fe-20Mn-2Ti alloy for long periods to precipitate Ti out of the matrix. Isothermal overaging at 800°C for 20 days left about 1% of the titanium in the matrix. The volume fraction of the ε phase increased again to 44% (Table III).

B. KINETICS AND MORPHOLOGY OF LAVES PHASE PRECIPITATION

1. Precipitation in the Fe-20Mn-2Ti Alloy:

Isothermal decomposition of the supersaturated solid solution quenched from the solution annealing temperature resulted in a hardness increase. The influence of temperature on the aging kinetics is shown in Fig. 4. As expected, the lower the aging temperature, the longer the time required to reach maximum hardness. The hardening response of the alloy was very slow in the aging temperature range 700°C to 900°C; it took more than 100 hours to achieve the maximum hardness plateau. No secondary hardening was observed which suggests that only a single precipitation process occurred.

The precipitate morphology in the aged samples are shown sequentially in Fig. 5, Fig. 6, and Fig. 7, for the aging temperature 900°C, 800°C, and 700°C respectively. Upon aging at each temperature, precipitates nucleated first at grain boundaries and grew continuously until a heavy network was formed (Fig. 8a). Just before a significant hardness increase, some precipitates were observed within the grains. As the aging time increased, more and more precipitates formed inside each grain, with an accompanying hardness increase as shown in the age hardening curves.

Precipitates inside grains appeared to line up along γ and ε phases boundaries. In later aging stages, the continuous precipitates along grain boundaries began to break up and individual particles were found to be spheroidized (Fig. 8b).

Apparently the precipitation process in the alloy is highly heterogeneous. Large surface energy is expected for the interface between the precipitate and the matrix. Classical nucleation theory [21] has pointed out that the critical energy required for the nucleation of second phase is significantly reduced if the nucleation occurs at high energy grain boundaries. The reason why precipitates formed continuously along grain boundaries is then trivial. The allignment of precipitates inside grains along the seemingly old γ-ε interfaces is also in agreement with the above hypothesis. Though the γ-ε interfaces do not exist when the alloy was heated up to the aging temperature which is greater than A_f (~240°C), the distortion energy due to the martensitic transformation might still remain [22] to help the nucleation of precipitation. The mechanism of spheroidization for the grain boundary precipitate at late aging stages needs further study; the precipitate growth and coarsening might play an important role in this phenomenon.

2. Precipitation in the Fe-28Mn-2Ti Alloy:

The hardness results for different aging temperatures are shown in Fig. 9. A similar age hardening response as that observed in the Fe-20Mn-2Ti alloy indicates that the same kind of precipitation reaction took place. The aging response is more temperature dependent in this completely austenitic alloy. The hardness approaches its plateau within 100 hours at 900°C; but there was no obvious hardness increase in a sample aged at 700°C for more than 200 hours. Though the as-annealed hardness

varied in two alloys (R_B72 for Fe-20Mn-2Ti and R_B62 for Fe-28Mn-2Ti). The total hardness increase at the plateau is the same (~R_B20). The hardness result can be explained by the morphology and distribution of precipitates. Fig. 10, Fig. 11, and Fig. 12 show the sequential microscopy of samples aged at various temperatures. In the early stage continuous precipitates rapidly developed along grain boundaries but contributed no hardness increase. The continuous precipitates can also be found along the incoherent interfaces of annealing twins; but few precipitates occurred on coherent interfaces. This also supports the hypothesis that the precipitation occurs in a heterogeneous manner which favors formation on high energy surfaces. Random nucleation started inside grains when most of the high energy surface are utilized. The hardness gradually increased as the percentages of precipitates observed in grains increased. Spheroidization of grain boundary precipitates was also observed during the final stage of aging (Fig. 13).

C. PRECIPITATE IDENTIFICATION

Samples of both alloys were aged at 800°C for 20 days to obtain precipitate sizes and volume fractions adequate for analysis. It is necessary to obtain precipitates with diameters greater than 2μ for EDAX analysis; and more than 5 volume pct for x-ray diffraction.

Many extra diffraction peaks were detected in the x-ray diffraction patterns (Fig. 14). Their corresponding interplanar spacings and relative intensities are listed in Table IV. These closely match the values in ASTM Powder Diffraction File for Fe_2Ti.[23] The crystal structure of the precipitate is the hexagonal Laves phase ($MgZn_2$ type, C14); each unit cell consists of 12 atoms as sketched in Fig. 15. The "a" parameter of the precipitate was determined from the (h k 0) reflections,

using the extrapolation function of Nelson and Riley.[24] The "c" parameter was determined from the (00ℓ) reflection by the method of Taylor and Floyd[25] for hexagonal crystals. The values obtained are a=4.780Å, c=7.788Å, and c/a=1.629.

To obtain the information about the chemical composition of the precipitates a SEM-EDAX study was made. Overetched specimens were examined in the scanning electron microscope, and some large precipitates (~5μ diameter) were chosen for EDAX analysis. Fig. 16 and Fig. 17 are comparative energy spectrums showing that precipitates are rich in titanium, and that they also contain manganese. The data converted by computer are given in Table V. The results are almost the same for both alloys. The fraction of Fe in the precipitates is about 2/3, while that of the sum of Mn and Ti is about 1/3. The extraction replicas of specimens were also made in order to avoid the influence of the matrix phase during EDAX analysis. The results confirmed the above observations. The identity of the precipitates thus appears to be $Fe_2(Ti, Mn)$ in both alloys. The crystal structure of precipitates is like that of Fe_2Ti, with Mn atoms sitting at some Ti lattice sites. There also exists the possibility that small fraction of Mn atoms replace Fe atoms in the precipitates. This is why the measured Fe concentration is somewhat less than the ideal stoichiometric ratio 2/3.

D. EFFECTS OF COLD WORK ON PRECIPITATION

It is not surprising that direct precipitation of Laves phases does not strengthen the solution-treated Fe-Mn-Ti austenites significantly. The interparticle spacing between the simply aged precipitates formed inside grains is too large to be an effective

obstacle to dislocation motion. The reasons for this ineffective precipitation are:

1. The alloys do not have enough beneficial nucleation sites for precipitation of Laves phase. The nucleation sites are not uniformly distributed throughout the grains.

2. Continuous precipitates which formed along grain boundaries dissipated a great amount of supersaturation at the early stage of aging. In-order to overcome these problems, about 50% reduction by cold rolling was conducted on both alloys between the solution annealing and the aging processes.

The mechanical instability of high Mn austenites has been investigated by many previous workers. [1,3,4] They will undergo a partial martensitic phase transformation under heavy deformation. In addition to the increase of defect and dislocation density, cold work induces elastic and plastic strain energy which raises the transformation temperature to the ambient temperature. The volume fraction of induced phases in the cold-worked samples is shown in Table III.

A large amount of the α' phase and some ε phase appeared in the Fe-20Mn-2Ti alloy due to cold rolling. The interesting microstructure is shown in Fig. 18, where the subgrains of irregular shape lie in array. Electron microscopy revealed that the induced α' phase is dislocated martensite with a high density of dislocations inside the martensite lathes (Fig. 19). Thin sheets of induced ε phase were also observed on edge parallel to one another.

On the other hand, there is some ε phase formed in the Fe-28Mn-2Ti alloy after cold working, but no α' phase was observed. The morphology of the mechanically induced ε phase (Fig. 20) is somewhat different

from the straight ε-sheet formed on cooling. These induced ε sheets look wavy and bent somehow, though they are parallel to one another in series. More detailed examination by electron microscopy verified the above observation (Fig. 21). High dislocation densities were observed in the untransformed matrix.

Like the usual martensite obtained by thermal treatment, the induced phase, ε or α', in the cold worked alloys was reverted to austenite when the sample was reheated to high temperature. The dilatometry results indicated that A_f is approximately 540°C. The subsequent quenching gave almost the same phase relation as that of a sample quenched from solution annealing temperature.

The Fe-20Mn-2Ti alloy was reheated to 800°C after cold-rolling, and then aged at that temperature. The kinetics of precipitation is accelerated by pre-deformation; very fine precipitates of Laves phase covered the entire structure in one hour aging (Fig. 22a). The precipitates were randomly distributed throughout the whole specimen, no continuous precipitate along grain boundaries was found. Very low diffusivity of the substitutional elements, Mn or Ti, in the present austenite matrix makes precipitate growth or coarsening very difficult. No evidence of overaging was observed even after aging for 96 hours (Fig. 22b). The metallographic results previously discussed can be correlated to the hardness curve shown in Fig. 23. The hardness of the alloy decreased quickly at the early stage, then slowly, and finally approached a constant value (~R_c26) (Fig. 23). The first drop in

hardness is due to the recovery of defects introduced during cold work; and the final constant hardness is attributed to the fine, randomly distributed precipitates. Absence of a hardness peak indicates that the full aged condition was reached in the very early stages of aging.

Closer examination of the precipitates formed in the cold worked plus aged alloys was carried out using the electron microscope. Selected area diffraction (SAD) patterns showed that the precipitates did not seem to have a special orientation relationship with the matrix (Fig. 24). Heavy deformation of the alloys before aging will distort the matrix causing precipitate misorientation with respect to one another even though the Laves phase has a characteristic orientation with the austenite. In the Fe-28Mn-2Ti alloy, the precipitates lined up along a specific orientation, which was the trace of the previous induced ε-phase. The precipitate size was less than 0.3μ in diameter. A high density dislocations still remained in the matrix after aging for one hour at 700°C (Fig. 25). The precipitates formed in the Fe-20Mn-2Ti alloy was denser in number and more random in distribution. Lath boundaries of previous α' martensites were revealed by the precipitate somewhere, but no continuous networks were observed (Fig. 26).

E. MECHANICAL PROPERTIES

The stress-strain curves for both as-annealed alloys in uni-axial tensile testing are shown in Fig. 27. A low yield strength and high elongation is the common feature of austenitic steel. The phase relations of these broken tensile specimens analyzed by x-ray diffraction showed similar results as that for cold rolling; this implies that the mechanically induced transformation also occurs during tensile testing. In both stress-strain curves, the ultimate point, where the tensile

specimen started to neck, was delayed to a large elongation with very low strain hardening. The final fracture of the specimen occurred rapidly after passing the ultimate point. This is a typical feature of alloys with a mechanically induced transformation such as "TRIP" steels. The ultimate strength keeps increasing with increasing amounts of induced phase generated by deformation. Both induced phases, α' and ε, appear to have a higher strength and less ductility than the parent γ phase. A stress increment of about 20ksi higher tensile strength for the Fe-20Mn-2Ti alloy came from the fact that the α' martensite is much stronger than the ε-phase.

The directly aged specimens reached full-hardening at 800^{o}C for 100 hours. Their grains are relatively large, (200 ~ 500μ diameter), surrounded by a nearly continuous network of Laves phase. A large grain size and heavily decorated grain boundaries are both detrimental to the ductility. The intergranular fracture mode was observed in broken tensile specimens of both alloys (Fig. 28). No significant strengthening effect occurred due to the large interparticle spacing between the precipitates inside the grains. The yield strength increased by ~5ksi for the Fe-28Mn-2Ti alloy and ~10ksi for the Fe-20Mn-2Ti alloy.

The stress-strain curves of the alloys which were cold worked and aged at 700^{o}C for 1 hour are shown in Fig. 29 and Fig. 30 along with the cold worked results. The yield strength was observed to increase to 107ksi for the Fe-20Mn-2Ti alloy and 90ksi for the Fe-28Mn-2Ti alloy by use of a cold working plus aging treatment. The difference in yield strength in the two different alloys may come from the existence of ε-phase and the difference in the cold work plus aging process. Unlike the cold worked alloys which reached the ultimate point without much

plastic deformation, the cold work plus aging alloys exhibited retarded necking with very large uniform elongation. This is believed to be the result of mechanically induced transformation.

The yield strength, tensile strength, and elongation of alloys with the cold work plus aging process are shown in Fig. 31 and Fig. 32 as a function of aging temperature. For one hour aging times, both alloys revealed a monotonically decreasing yield strength for increasing aging temperature. The elongation showed a peak in the temperature range $650^{o}C$ to $800^{o}C$. A similar result was observed in the thermal cycling processing of the TRIP steel.[24] The influence of aging time on yield strength and elongation are shown in Fig. 33. No obvious change in elongation was observed for aging times up to 4 hours, although the yield strength kept decreasing with aging time. The fracture surface of the broken tensile specimen was unusual. It was neither the dimpled rupture of ductile failure like the as-annealed (Fig. 34) or the cold worked samples (Fig. 35) nor the intergranular cleavage of brittle fracture (Fig. 28). In the Fe-20Mn-2Ti alloy, in which $\gamma \rightarrow \alpha'$ martensite transformation is predominant, a flat fracture surface almost perpendicular to the tensile axis was formed. Very tiny cups and cones spread over the whole fracture surface (Fig. 36). On the other hand, the Fe-28Mn-2Ti alloy, in which only the $\gamma \rightarrow \varepsilon$ transformation occurred, exhibited a fracture surface consisting of several tilted planes. In addition to the dimple rupture, a lamellar pattern was observed (Fig. 37). The exact mechanism responsible for these fracture surfaces has not been established.

Contrary to expectations from the high tensile elongation, the Charpy impact energy for the worked and aged specimen was quite low.

Fig. 38 shows the impact toughness C_v as a function of aging temperature (1 hours) for both alloys. In the Fe-20Mn-2Ti alloy, all the aged samples have lower impact energy than the cold worked one (34 ft-lb). The higher aging temperature made the impact toughness increase, approaching that of the cold worked one. Conversely, the impact energy of the Fe-28Mn-2Ti alloy became higher after aging, and decreased back to that of the cold worked specimen (~40 ft-lb) with increasing aging temperature. Further study is needed to understand the exact mechanisms occurring during testing.

IV. CONCLUSION

1. Precipitation in the Fe-20Mn-2Ti and Fe-28Mn-2Ti systems proceeds by the formation of single particles of equilibrium Laves phase, $Fe_2(Mn,Ti)$, hexagonal C14 type ($MgZn_2$). No transition phases were detected.

2. Precipitation in the as-annealed structure occurs by heterogeneous nucleation; heavy networks of Laves phases form first along the grain boundary before individual precipitates appear inside grains. No significant age hardening is observed but intergranular fracture takes place due to the Laves phase precipitates.

3. Cold rolling after solution annealing provides numerous efficient nucleation sites for beneficial subsequent aging. A desirable microstructure, in which fine precipitates are randomly distributed, is then obtained.

4. Enhancement of the mechanical properties of Fe-Mn austenities can be achieved through the combination of cold work, fine precipitates, and mechanically induced transformation.

5. Titanium additions can stabilize the austenite of Fe-Mn alloys.

ACKNOWLEDGEMENTS

The author would like to express his gratitude to Professor John W. Morris, Jr. for his continuous guidance and encouragement during this investigation. This research was performed partially under the auspices of the Energy Research and Development Administration through the Materials and Molecular Research Division of the Lawrence Berkeley Laboratory and partially under Grant NGR 05-003-526 of NASA Lewis Research Center.

REFERENCES

1. C. H. White and R. W. K. Honeycombe, J. Iron Steel Inst., 1962, Vol. 200, p. 457.
2. V. F. Zackay, E. R. Parker, D. Fahr, and R. Bush, Trans. ASM, 1967, Vol. 60, p. 252.
3. D. J. Drobjak and J. Gordon Parr, Met. Trans., 1970, Vol. 1, p. 1521.
4. K. Sipos, L. Remy, and A. Pineau, Met. Trans., 1976, Vol. 7A, p. 857.
5. R. Franks, W. Binder, and J. Thompson, Trans. ASM, 1955, Vol. 47, p. 231.
6. J. A. Douthett, Metal Progr., 1975, Vol. 108, No. 3, p. 50.
7. Metal Progr., 1976, Vol. 110, No. 5, p. 72.
8. M. V. Nevitt, Electronic Structure and Alloy Chemistry of the Transition Elements, (Interscience Publishers, New York, 1963, p. 101).
9. K. Bungardt and G. Lennartz, Arch. Eisenhuttenw, 1962, Vol. 33, p. 251.
10. S. Jin, "Spheroidization of the Grain Boundary Precipitates in Fe-Ta-Cr Alloys' M.S. Thesis, Univ. of California, 1971.
11. M. Hansen, "Constitution of Binary Alloys", McGraw-Hill, New York, 1958.
12. E. M Sokolovskaya, A.T. Grigorév, and Yu. F. Altunin, Russ. J. Inorg. Chem., 1962, Vol. 7, p. 1464.
13. E. Orowan, "Symposium on Internal Stress", Inst. of Metals, London, 1947. p.451
14. J. E. Bailey, Phil. Mag., 1960, Vol. 5, p. 833.
15. B. D. Cullity, Elements of X-Ray Diffraction, (Addison-Wesley, California, 1956, p. 388.)
16. H. Schumann, Arch. Eisenhuttenw, 1967, Vol. 38, p. 647.
17. A. Holden, J. d. Bolton, and E. R. Petty, J. Iron Steel Inst., 1971, Vol. 209, p. 721.
18. S. Barnartt, R. Stickler, and D. van Rooyen, Corrosion Sci., 1963, Vol. 3, p. 9

19. R. B. G. Yeo, Trans. TMS-AIME, 1963, Vol. 227, p. 884.

20. J. K. Abraham and J. S. Pascover, Trans. TMS-AIME, 1969, Vol. 245, p. 759.

21. P. J. Clemm and J. C. Fisher, Acta Met., 1955, Vol. 3, p. 70.

22. G. Krauss, Jr. and M. Cohen, Trans, TMS-AIME, 1962, Vol. 224, p. 1212.

23. G. R. Speich, Trans. TMS-AIME, 1962, Vol. 224, p. 850.

24. T. J. Koppeneal, Met. Trans., 1972, Vol. 3, p. 1549.

Table I

OCCURRENCE OF PHASES IN BINARY AND TERNARY TRANSITION ELEMENT SYSTEMS

B Transition Element	A Element: Group IV (4e/a)			Group V (5e/a)			Group VI (6e/a)			BB'
	Ti	Zr	Hf	V	Nb	Ta	Cr	Mo	W	
Mn (7e/a)	B_2A Chi Sigma	B_2A Chi	B_2A Chi	BA Chi Sigma	B_2A Chi	B_2A Chi	Chi Sigma	Chi Sigma	Chi	
Fe (8e/a)	B_2A BA Chi	B_2A	B_2A	BA Chi Sigma	B_2A Sigma	B_2A Sigma	Sigma	B_2A Mu Chi Sigma	B_2A Mu	FeAl FeCo
Co (9e/a)	B_2A BA G	B_2A BA G	B_2A BA G	B_3A Chi Sigma	B_2A G	B_2A G	Sigma	B_3A Mu Sigma	B_3A Mu	CoAl
Ni (10e/a)	B_3A BA G	G	G	B_3A Chi Sigma G	B_3A Mu G	B_3A Mu G	Sigma	B_3A		Beta (NiAl)

Table II. CHEMICAL COMPOSITION OF ALLOYS

Ingot No.	Weight	Designation	Composition wt%		
			Fe	Mn	Ti
755-1	23 lb.	Fe-20Mn	Bal.	19.11	--
755-2	23 lb.	Fe-20Mn-2Ti	Bal.	18.66	1.70
7511-4	10 lb.	Fe-28Mn-2Ti	Bal.	27.29	1.59
7511-10	10 lb.	Fe-28Mn	Bal.	27.34	--
766-17	23 lb.	Fe-20Mn-2Ti	Bal.	19.07	1.74
766-18	23 lb.	Fe-28Mn-2Ti	Bal.	27.93	1.69

*The impurity levels: C = 0.004%; N = 0.002%; O = 0.002%; P = 0.004%; Si $\leq$ 0.01%; S = 0.006%.

Table III. DETERMINATION OF VOLUME PERCENT OF PHASE PRESENT BY X-RAY ANALYSIS

Designation	Treatment	Phase volume percent		
		γ	ε	α'
Fe-20Mn	AN	30.0	70.0	--
Fe-20Mn-2Ti	AN	90.4	9.6	--
Fe-20Mn-2Ti	AN+800°C/20 days	56.0	44.0	--
Fe-20Mn-2Ti	AN+CW	51.0	20.0	29
Fe-20Mn-2Ti	AN+CW+800°C/96 hrs	91.2	8.8	--
Fe-28Mn	AN	95.0	5.0	--
Fe-28Mn-2Ti	AN	100.0	--	--
Fe-28Mn-2Ti	AN+800°C/20 days	100.0	--	--
Fe-28Mn-2Ti	AN+CW	95.0	$\lesssim$5.0	--
Fe-28Mn-2Ti	AN+CW+700°C/1 hr	100.0	--	--

AN: Annealed at 1150°C for 1-1/2 hr.

CW: 50% reduction of cold rolling

Table IV. INTERPLANAR SPACING OF THE PRECIPITATES

Precipitates			(hkℓ)	Standard values for Fe_2Ti	
2θ*	d	I/I_1		d	I/I_1
--	--	--	100	4.133	10
--	--	--	002	3.889	10
--	--	--	101	3.649	10
37.6	2.390	30	110	2.388	30
41.0	2.199	90	103	2.199	100
--	--	--	200	2.068	10
44.4	2.039	90	112	2.038	100
45.3	2.001	100	201	1.998	100
46.6	1.947	40	004	1.947	30
49.85	1.828	20	202	1.828	30
51.8	1.763	10	104	1.760	10
--	--	--	203	1.620	10
--	--	--	300	1.382	10
70.2	1.339	40	123	1.341	60
72.65	1.330	40	006	1.302	60
76.4	1.246	30	205	1.247	60
--	--	--	124	1.223	10
80.25	1.195	40	220	1.196	60

*CuKα radiation with $\lambda = 1.54\text{Å}$

Table V. DETERMINATION OF CHEMICAL COMPOSITION OF THE PRECIPITATES BY EDAX

Designation		Concentration (wt%)		
		Fe	Mn	Ti
Fe-20Mn-2Ti	matrix	78.90	19.44	1.66
	precipitate	63.60	14.80	21.60
Fe-28Mn-2Ti	matrix	69.76	29.34	0.90
	precipitate	62.90	14.30	22.80

*Specimens were aged at 800°C for 20 days.

FIGURE CAPTIONS

1. Block diagram of the Energy Dispersive X-ray Analysis (EDAX) system.
2. Optical micrographs of as-annealed (a) Fe-28Mn and (b) Fe-28Mn-2Ti alloys. X1300
3. Optical micrographs of as-annealed (a) Fe-20Mn and (b) Fe-20Mn-2Ti alloys. X1300
4. Age hardening curves for the Fe-20Mn-2Ti alloy.
5. Optical micrographs of the Fe-20Mn-2Ti alloy aged at 900^{o}C for (a) 2 hrs (b) 8 hrs (c) 24 hrs and (d) 48 hrs. X160
6. Optical micrographs of the Fe-20Mn-2Ti alloy aged at 800^{o}C for (a) 2 hrs (b) 16 hrs (c) 48 hrs and (d) 165 hrs. X160
7. Optical micrographs of the Fe-20Mn-2Ti alloy aged at 700^{o}C for (a) 30 hrs (b) 124 hrs (c) 240 hrs. X160
8. Precipitates morphology of the Fe-20Mn-2Ti alloy at (a) early stage, 800^{o}C for 2 hrs (b) late stage, 800^{o}C for 48 hrs. X1300
9. Age hardening curves for the Fe-28Mn-2Ti alloy.
10. Optical micrographs of the Fe-28Mn-2Ti alloy aged at 900^{o}C for (a) 4 hrs (b) 16 hrs (c) 48 hrs. X225
11. Optical micrographs of the Fe-28Mn-2Ti alloy aged at 800^{o}C for (a) 34 hrs (b) 96 hrs. X225
12. Optical micrographs of the Fe-28Mn-2Ti alloy aged at 700^{o}C for (a) 48 hrs (b) 120 hrs. X225
13. Spheroidized graon boundary precipitates at late stage 800^{o}C for 96 hrs, of the Fe-28Mn-2Ti alloy. X1850
14. X-ray diffractometer trace of the Fe-28Mn-2Ti alloy aged at 800^{o}C for 20 days.
15. Atomic arrangement in the unit cell of the C14 ($MgZn_2$) crystal.

16. Scanning electron micrograph and the x-ray energy spectrum of the precipitate in the Fe-20Mn-2Ti alloy. X2500
17. Scanning electron micrograph and the X-ray energy sepctrum of the precipitate in the Fe-28Mn-2Ti alloy. X2500
18. Optical micrograph of the cold-worked Fe-20Mn-2Ti alloy. X1750
19. Transmission electron micrograph of the cold-worked Fe-20Mn-2Ti alloy. X12,000
20. Optical micrograph of the cold-worked Fe-28Mn-2Ti alloy. X1750.
21. Transmission electron micrographs of the cold-worked Fe-28Mn-2Ti alloy. X35,000
22. Optical micrographs of the cold-worked Fe-20Mn-2Ti aged at 800^{o}C for (a) 1 hr (b) 96 hrs. X1350
23. Age hardening curve (800^{o}C) of the cold-worked Fe-20Mn-2Ti alloy.
24. Selected area diffraction (SAD) of the precipitates formed in cold-worked alloys.
25. Transmission electron micrograph of the cold-worked Fe-28Mn-2Ti alloy aged at 700^{o}C for 1 hr. X20,000
26. Transmission electron micrograph of the cold-worked Fe-20Mn-2Ti alloy aged at 700^{o}C for 1hr. X20,000.
27. Engineering stress-strain curves of as-annealed alloys.
28. Scanning electron micrographs of the tensile fracture surface of the simple aged (a) Fe-20Mn-2Ti and (b) Fe-28Mn-2Ti alloy.
29. Engineering strain-stress curves of cold-worked and cold-worked plus aged Fe-20Mn-2Ti alloy.
30. Engineering strain-stress curves of cold-worked and cold-worked plus aged Fe-28Mn-2Ti alloy.
31. The effect of aging temperature (1 hr) on the strength and elongation of the cold-worked Fe-20Mn-2Ti alloy.

32. The effect of aging temperature (1 hr) on the strength and elongation of the cold-worked Fe-28Mn-2Ti alloy.
33. The effect of aging time (700^{o}C) on the yield strength and elongation of the cold-worked Fe-20Mn-2Ti alloy.
34. Scanning electron micrographs of the tensile fracture surface of (a) as-annealed and (b) cold-worked Fe-20Mn-2Ti alloy. X1300
35. Scanning electron micrographs of the tensile fracture surface of (a) as-annealed and (b) cold-worked Fe-28Mn-2Ti alloy. X1300
36. Scanning electron micrographs of the tensile fracture surface of the cold-worked Fe-20Mn-2Ti alloy aged at 700^{o}C for (a) 1 hr and (b) 4 hrs. X1300
37. Scanning electron micrographs of the tensile fracture surface of the cold-worked Fe-28Mn-2Ti alloy aged for 1hr at (a) 800^{o}C and (b) 700^{o}C. X1300
38. The effect of the aging temperature (1 hr) on the Charpy impact energy of the Fe-20Mn-2Ti alloy.

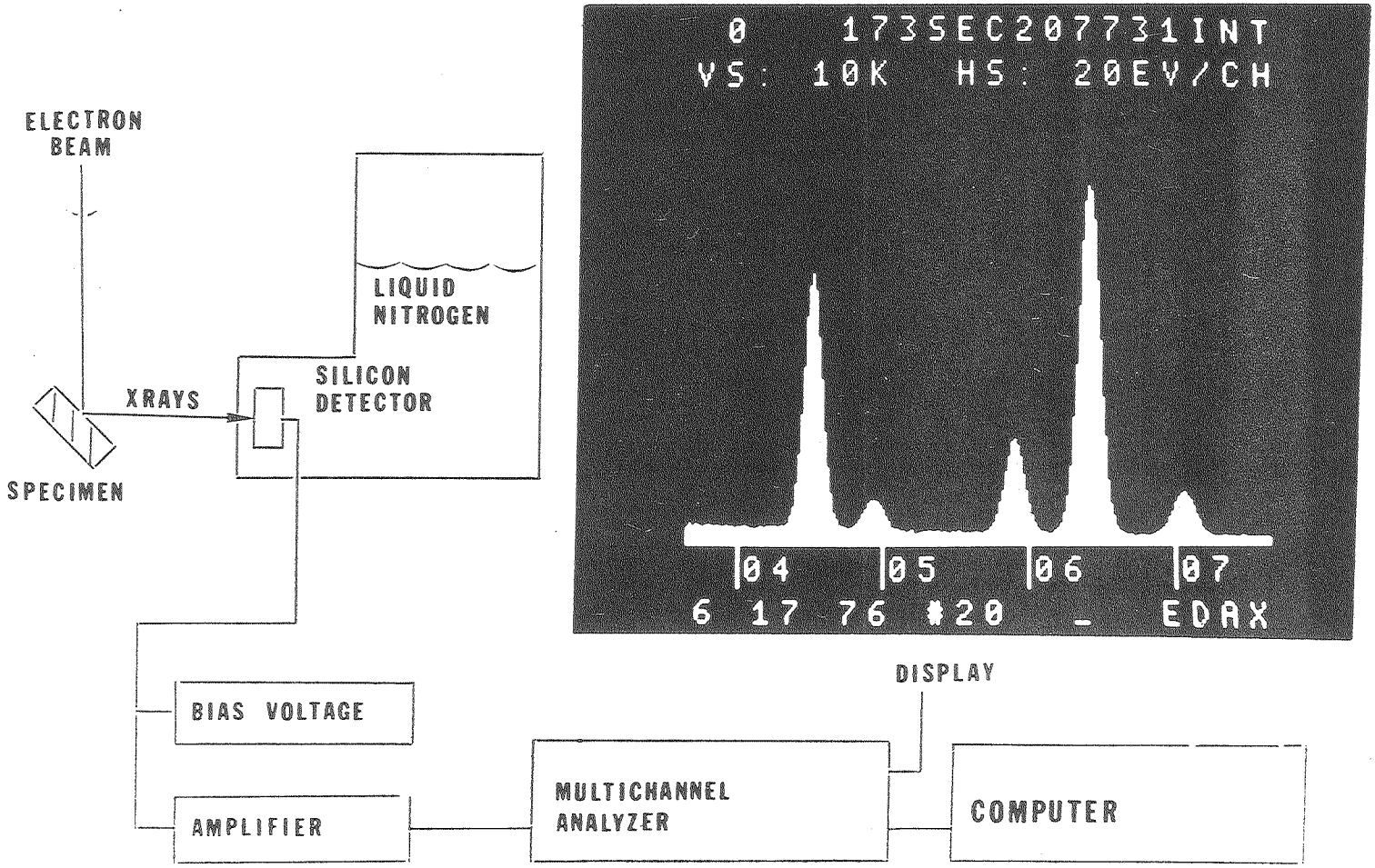

Fig. 1

XBB760-10434

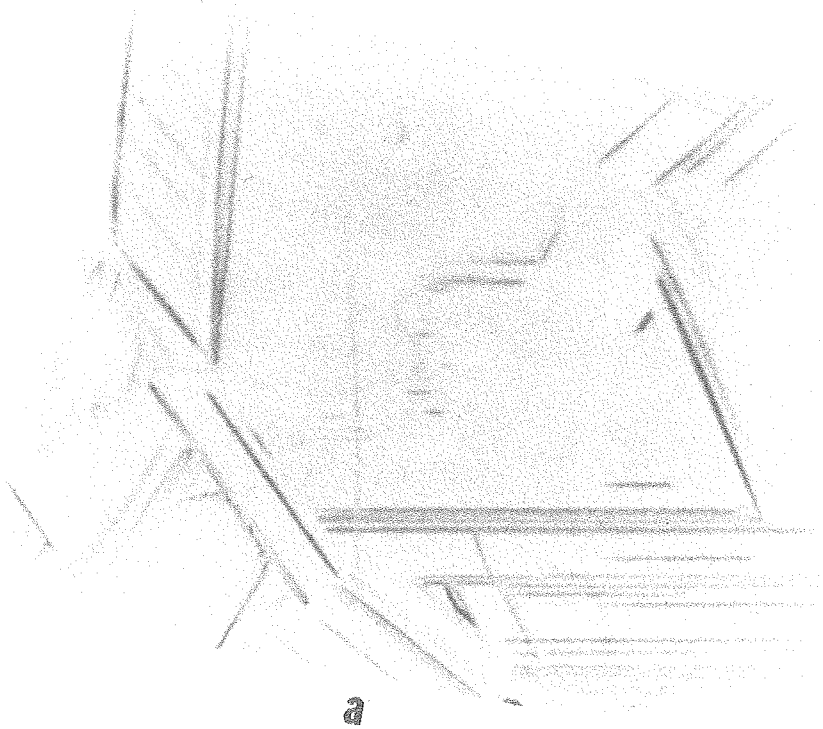

a

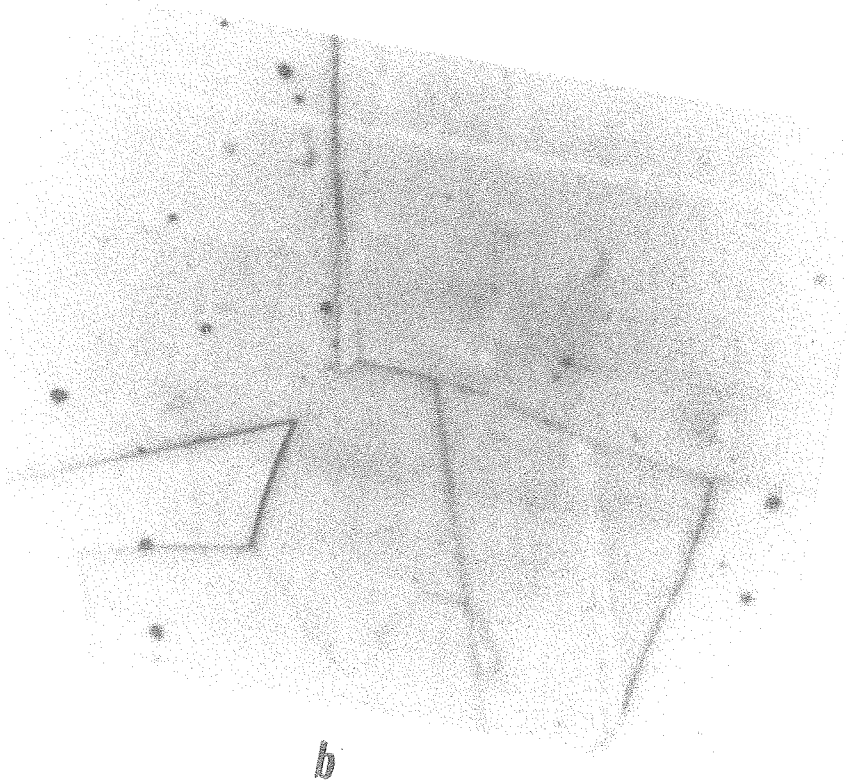

b

XBB760-10433

Fig. 2

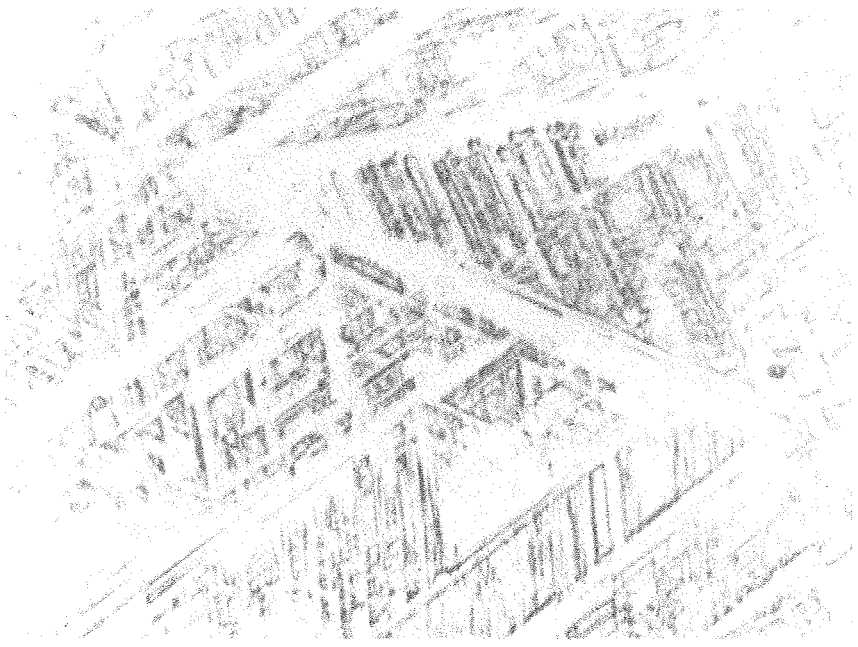

a

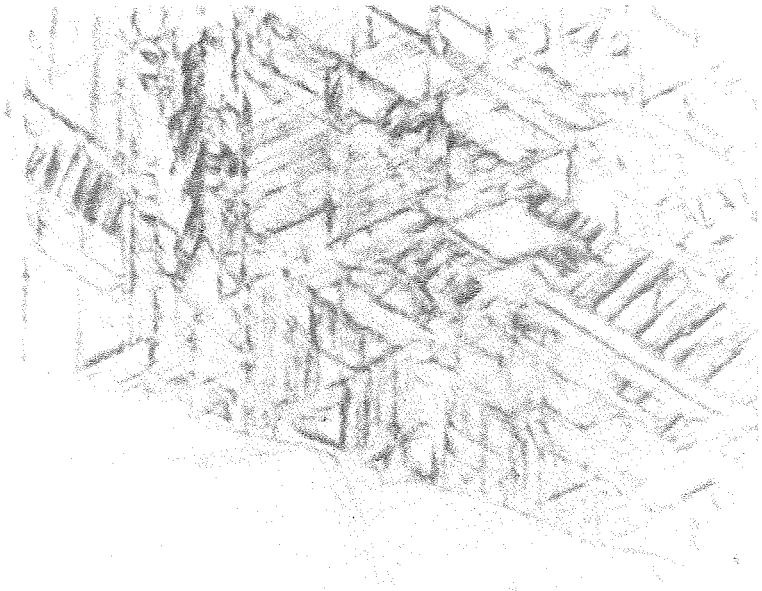

b

XBB769-8585

Fig. 3

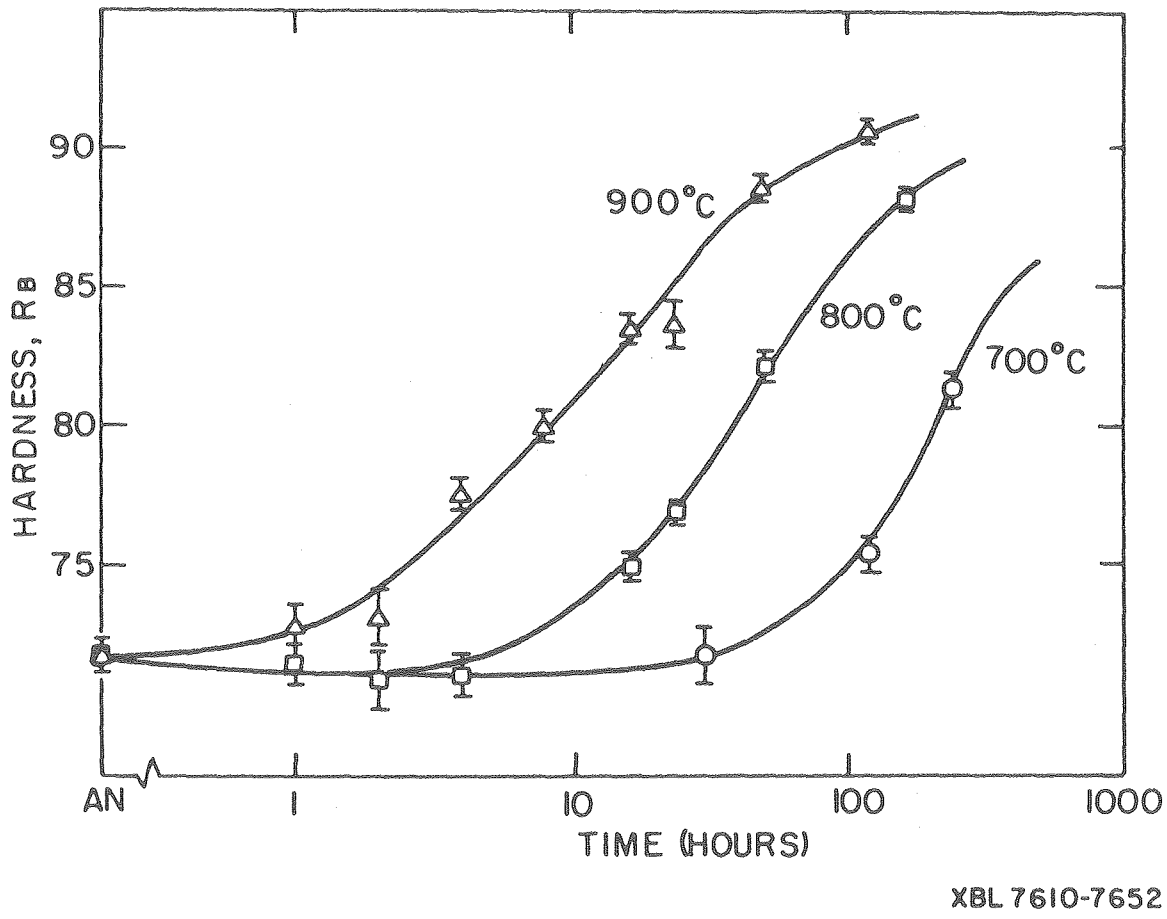

Fig. 4 . Age hardening curves for the Fe-20Mn-2Ti alloy.

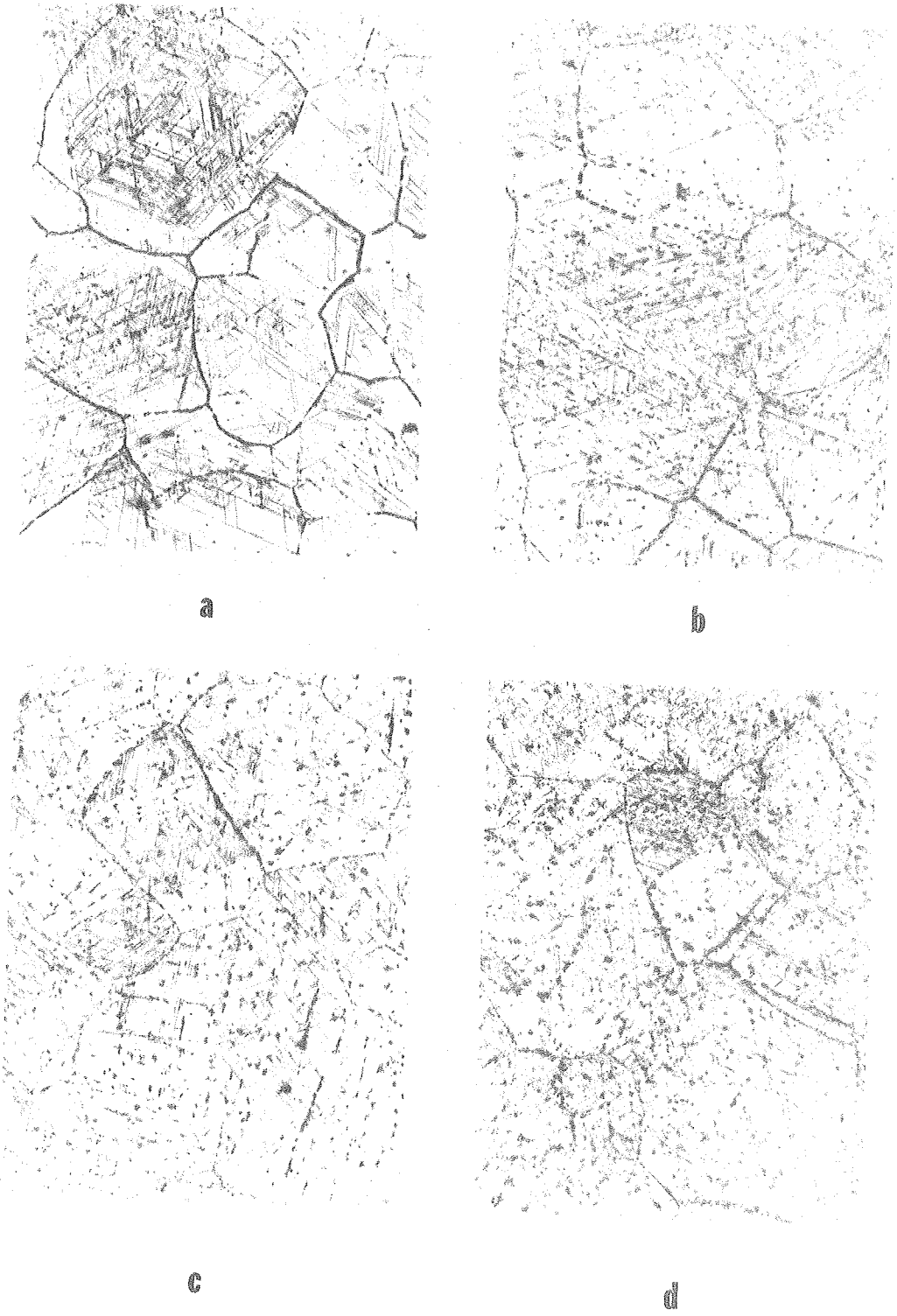

XBB769-8591

Fig. 5

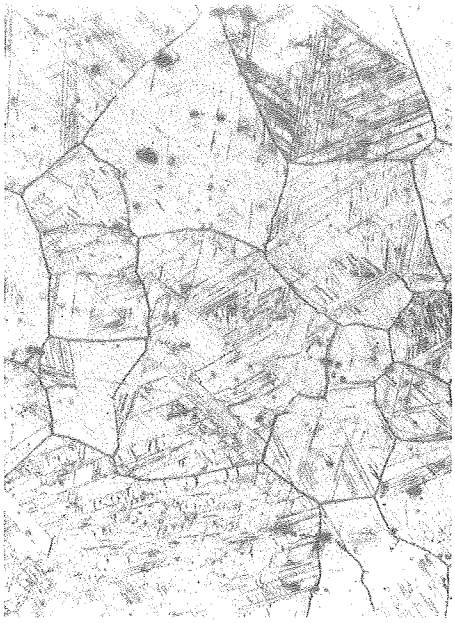

a

b

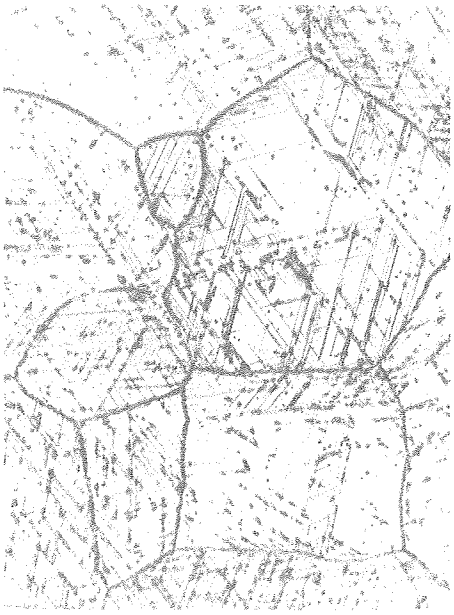

c

d

XBB769-8590

Fig. 6

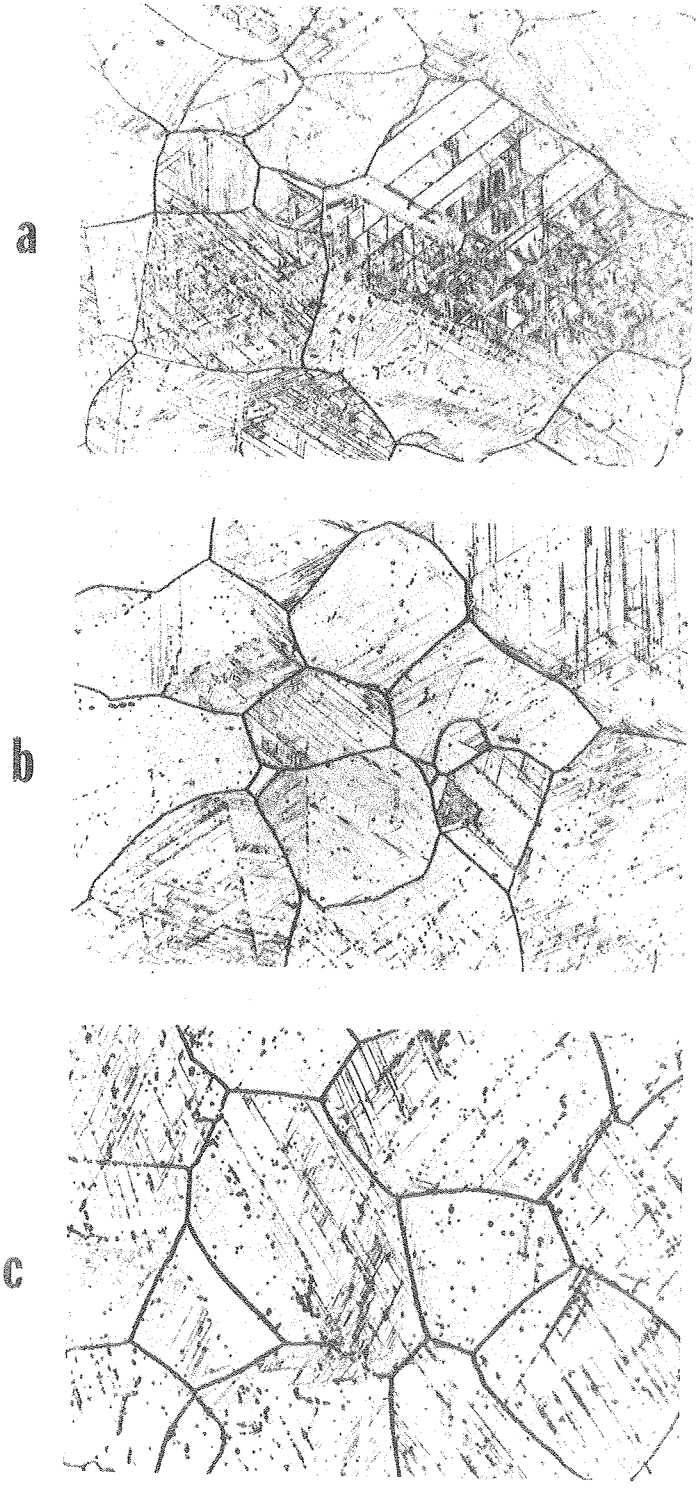

XBB769-8589

Fig. 7

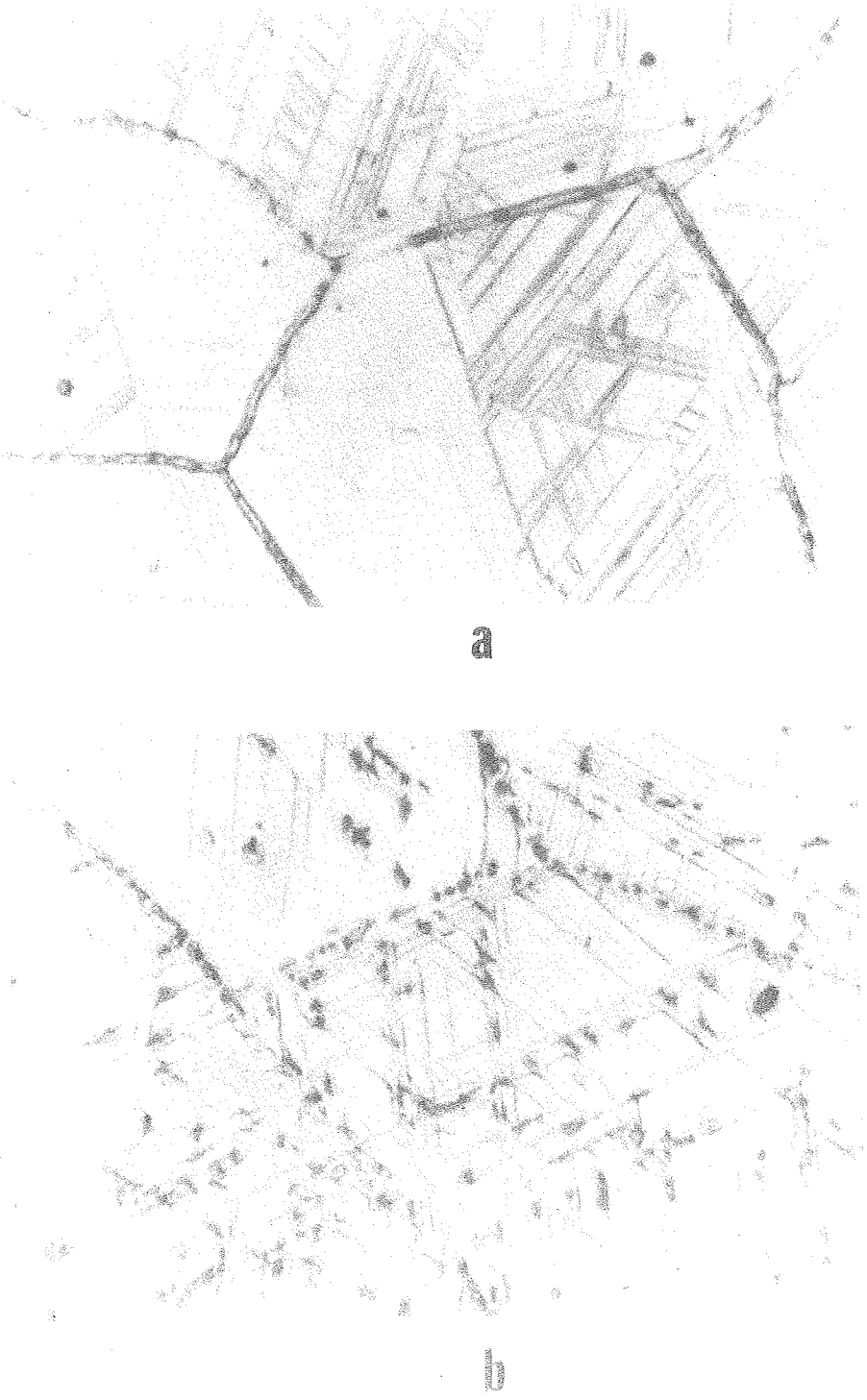

XBB769-8584

Fig. 8

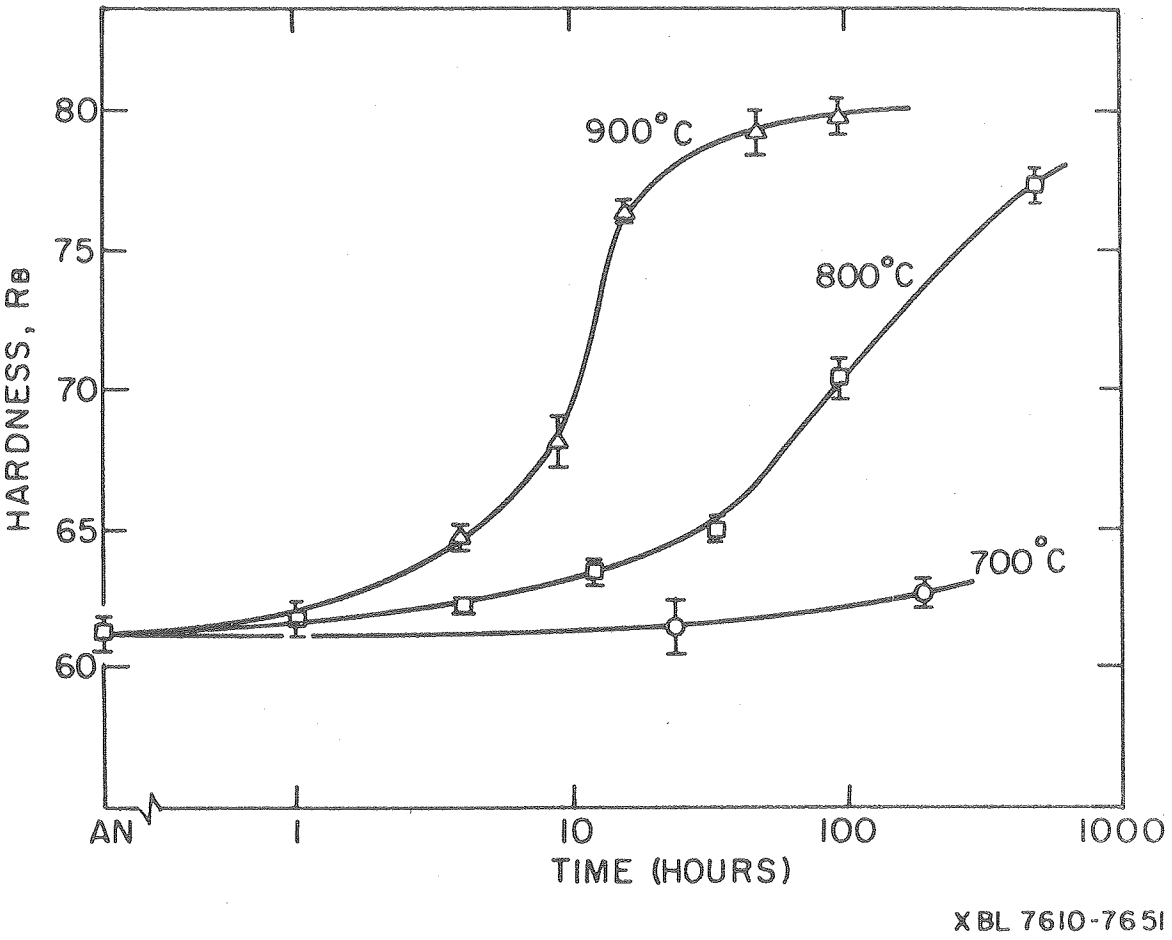

Fig. 9. Age hardening curves for the Fe-28Mn-2Ti Alloy

a

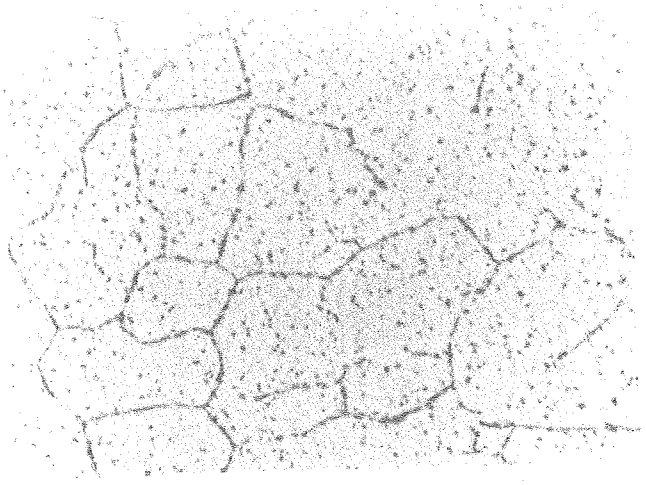

b

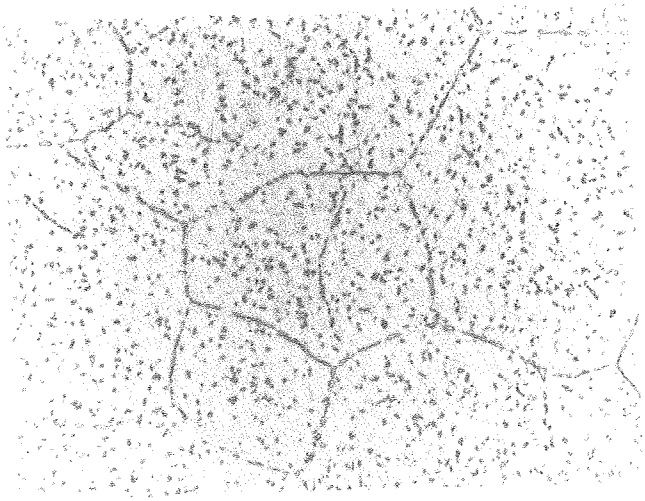

c

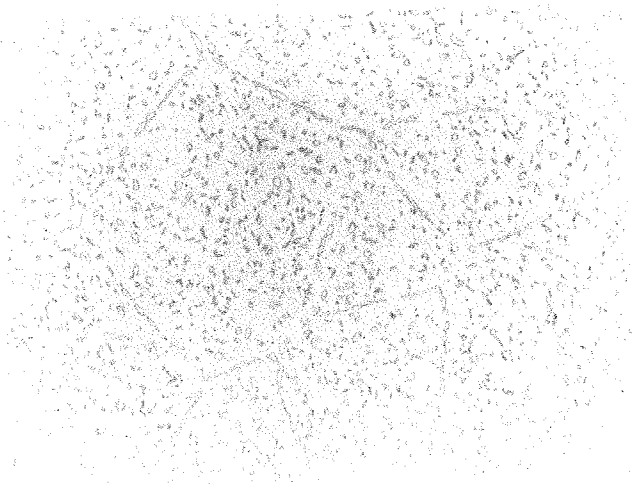

XBB760-10431

Fig. 10

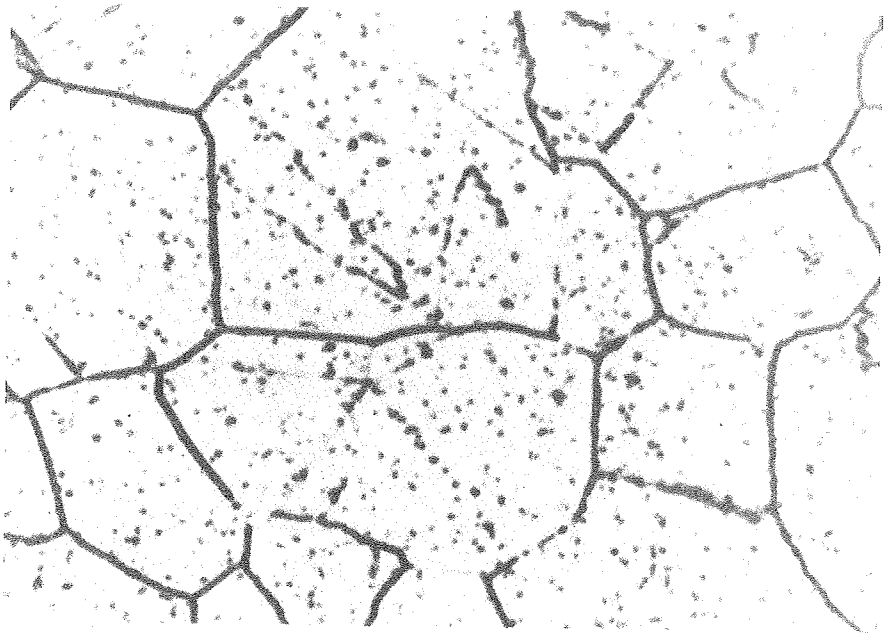

a

b

XBB769-8587

Fig. 11

XBB769-8588

Fig. 12

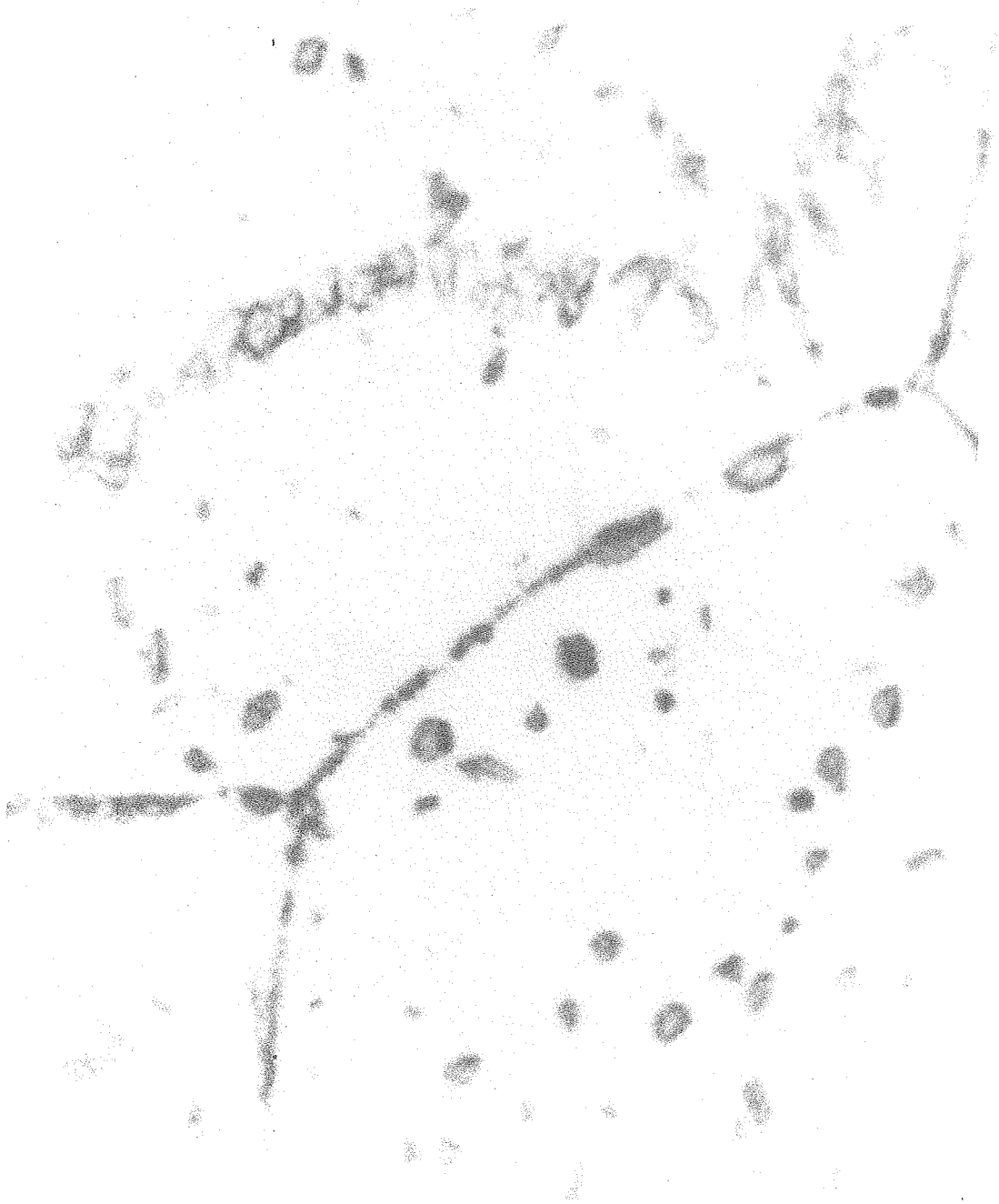

XBB769-8592

Fig. 13

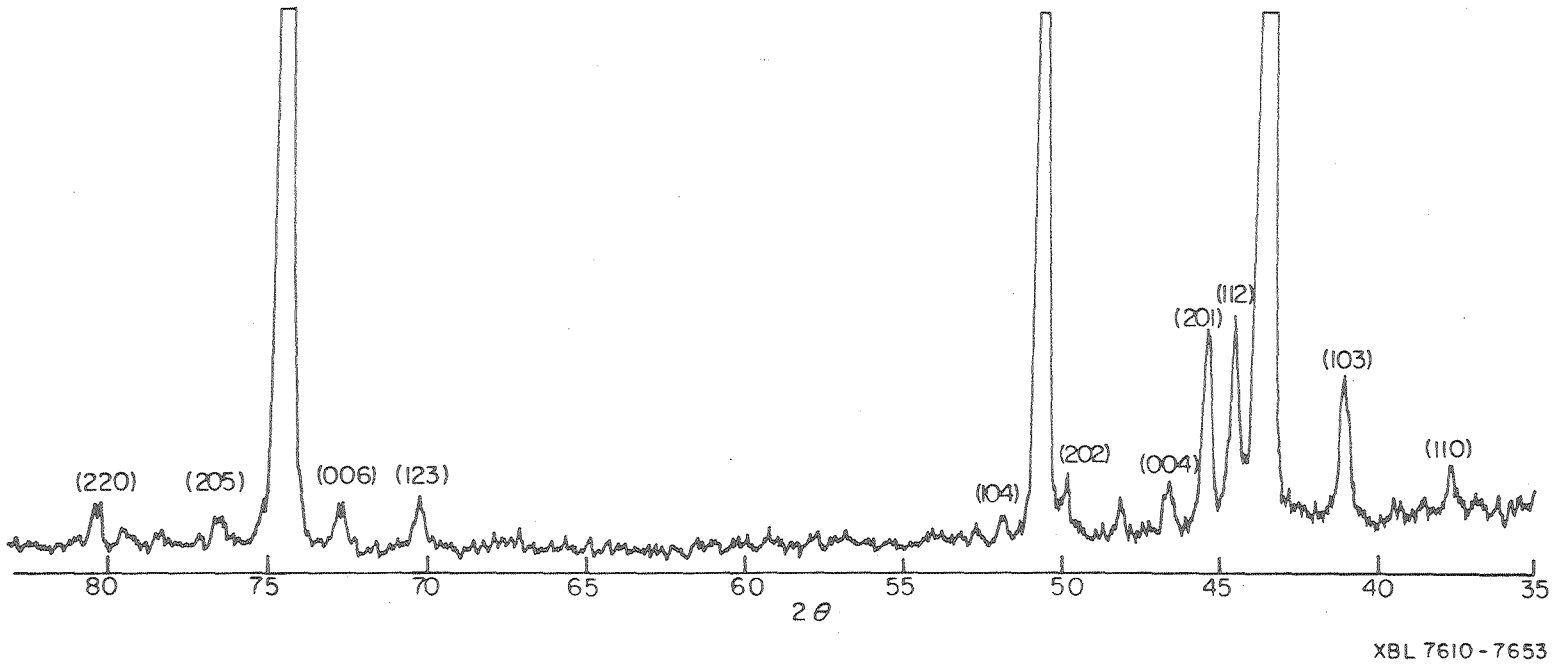

Fig. 14. X-ray diffractometer trace of the Fe-28Mn-2Ti alloy aged at 800°C for 20 days.

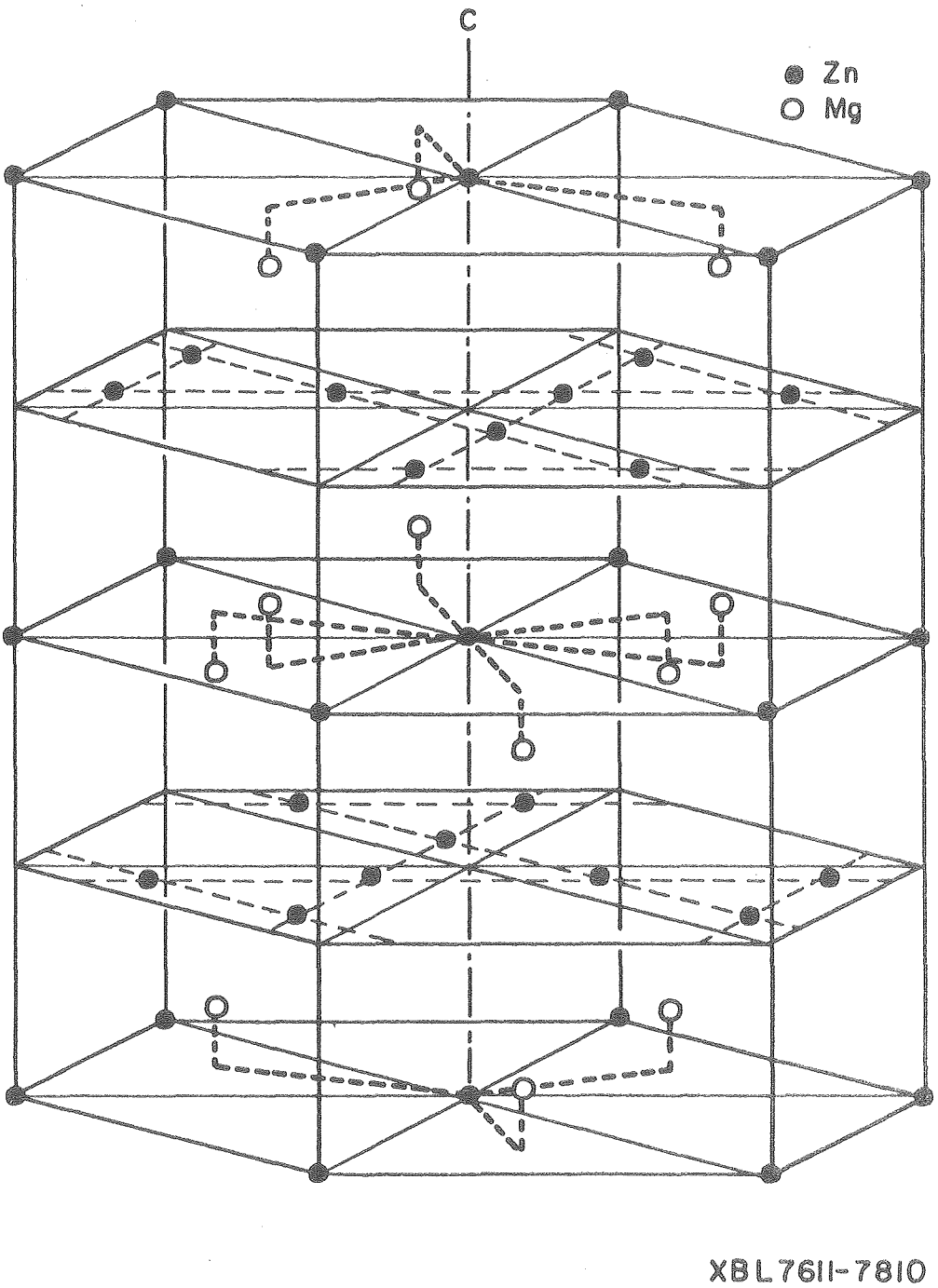

Fig. 15. Atomic arrangement in the unit cell of the C14 ($MgZn_2$) crystal.

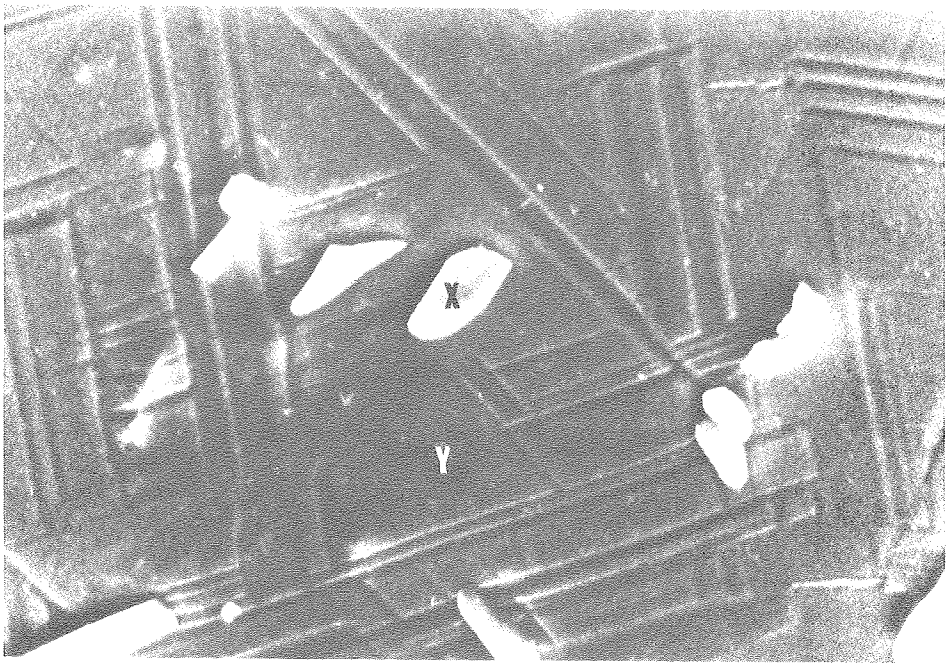

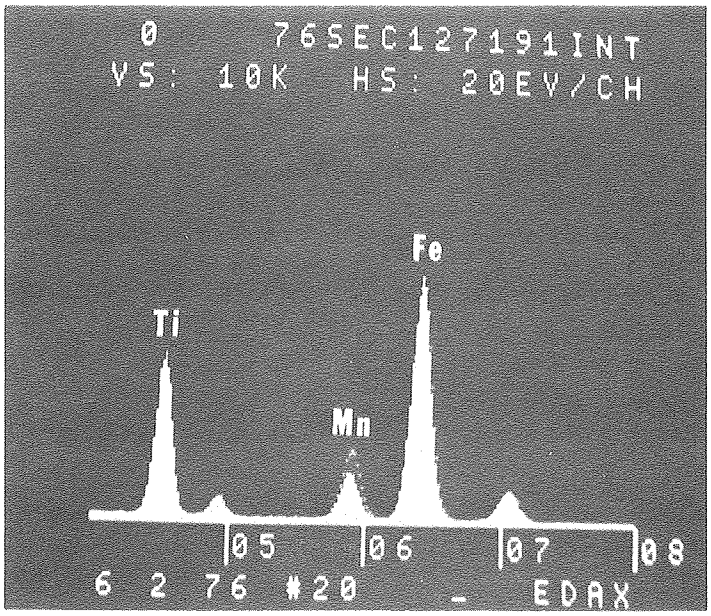

XBB769-8583

Fig. 16

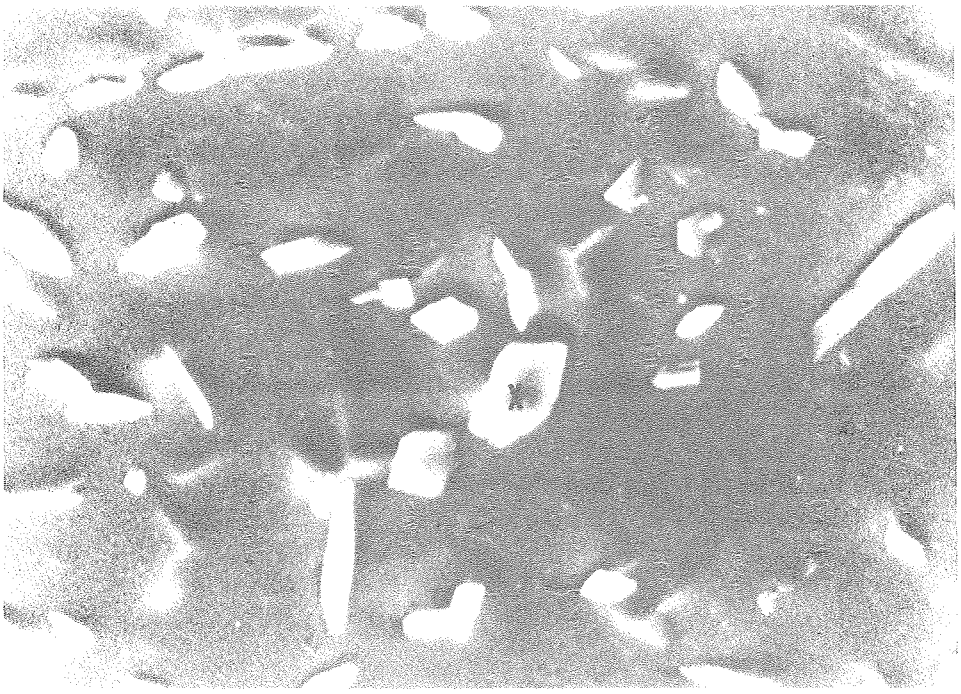

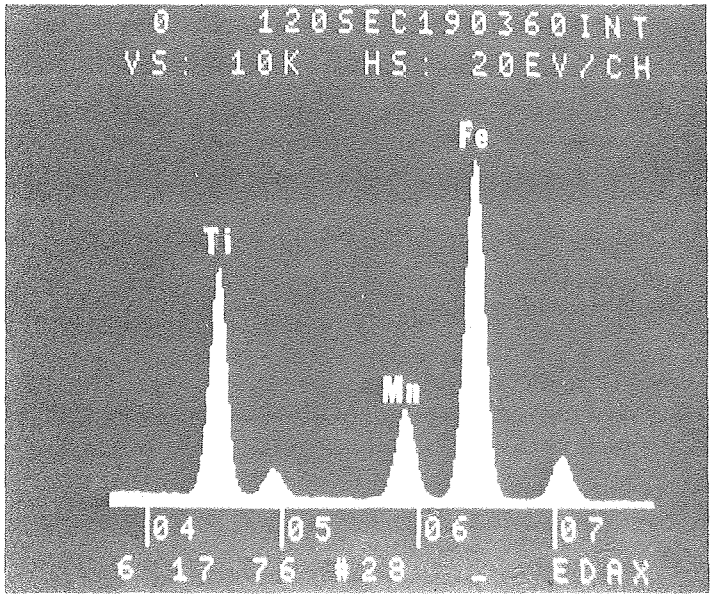

XBB769-8582

Fig. 17

XBB769-8593

Fig. 18

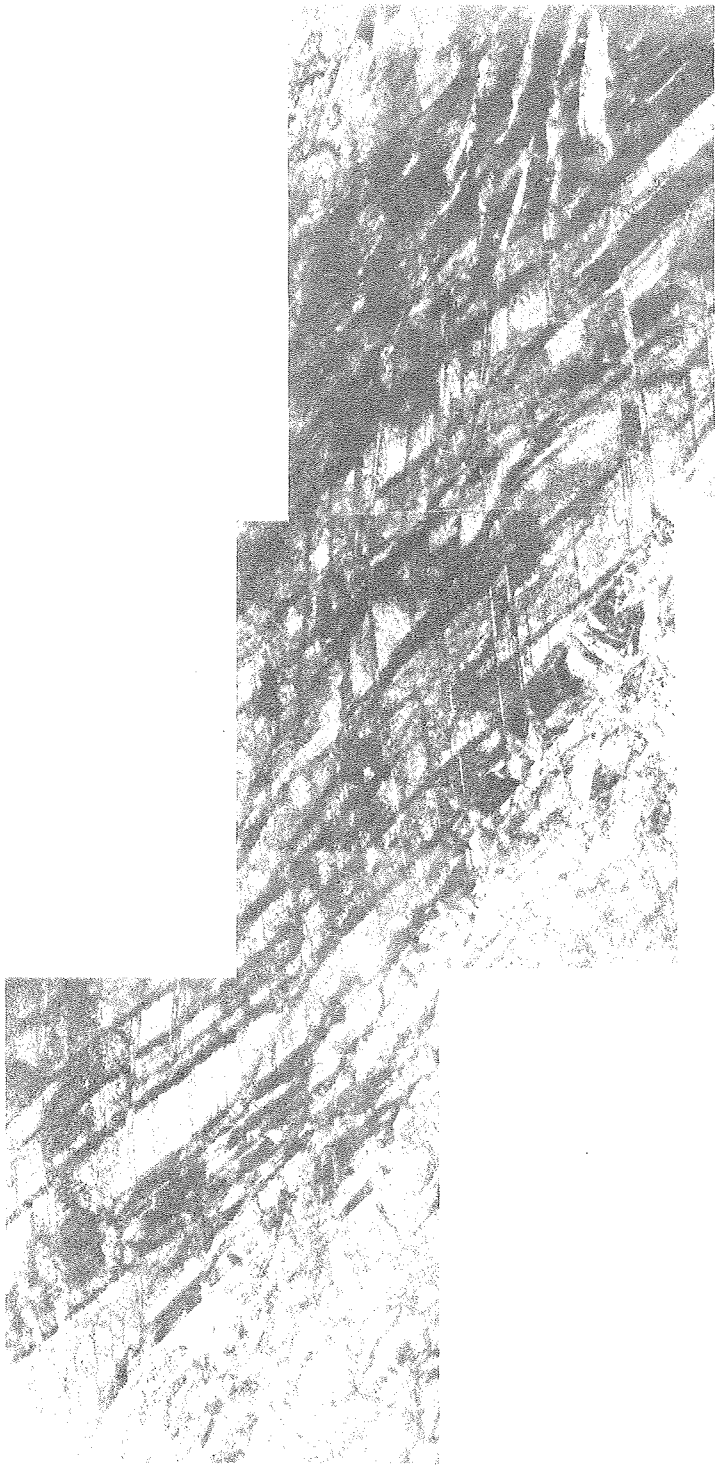

XB3773-1950

Fig. 19

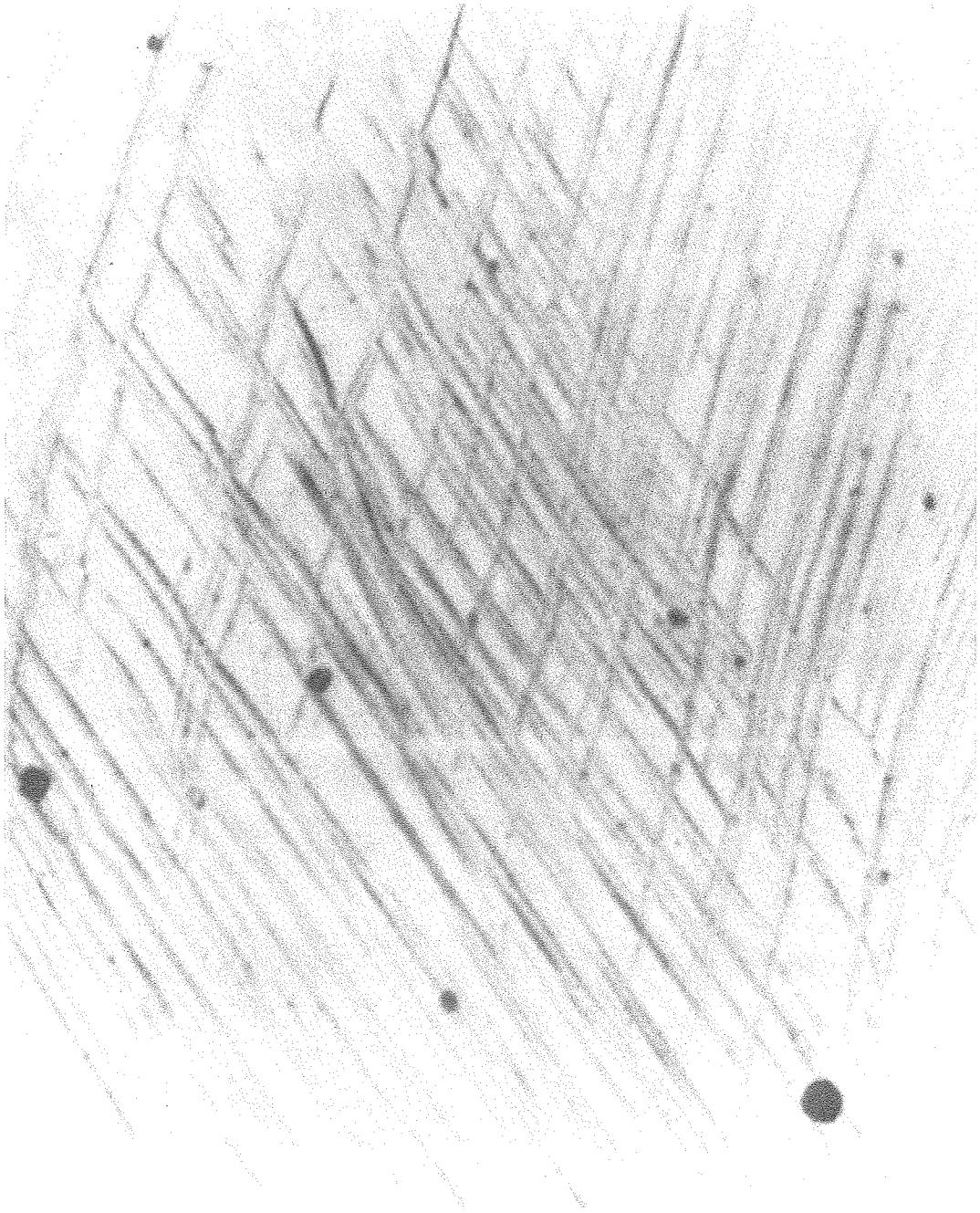

XBB760-10432

Fig. 20

DE

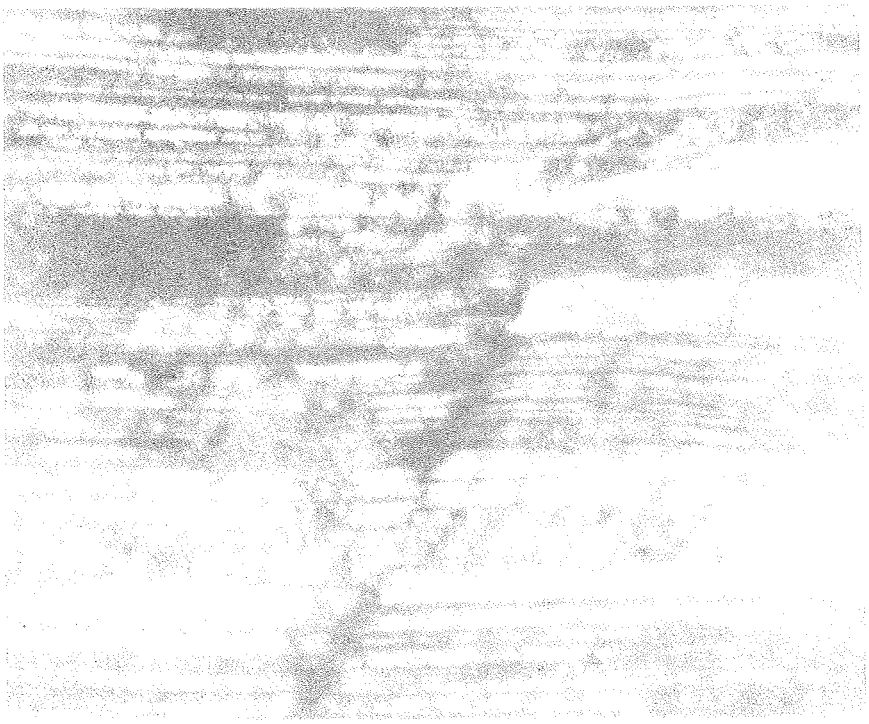

EA

Fig. 21

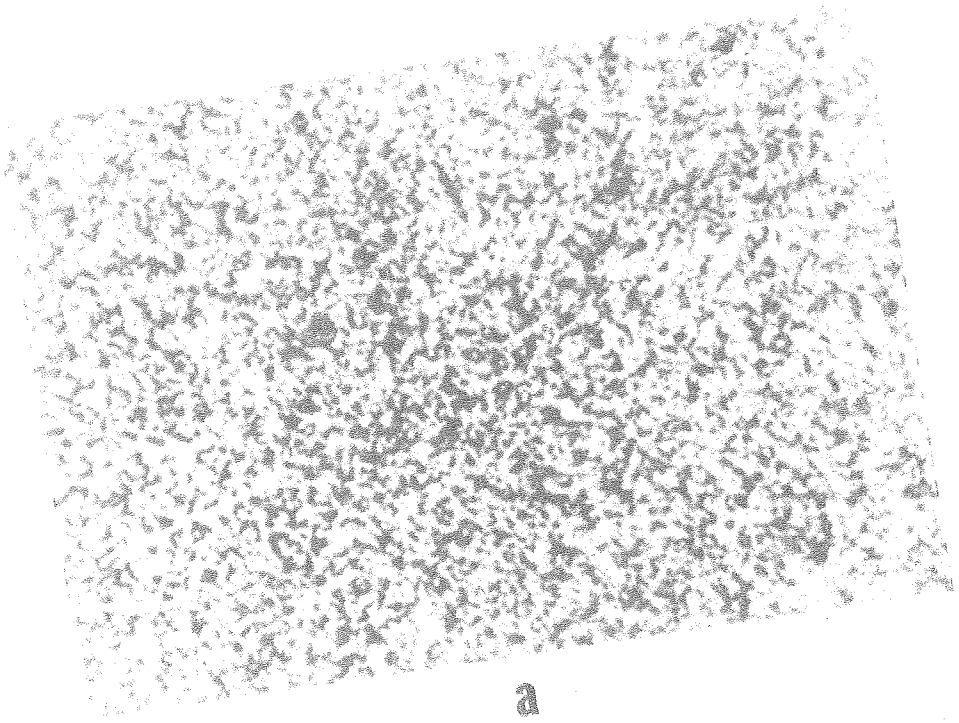

a

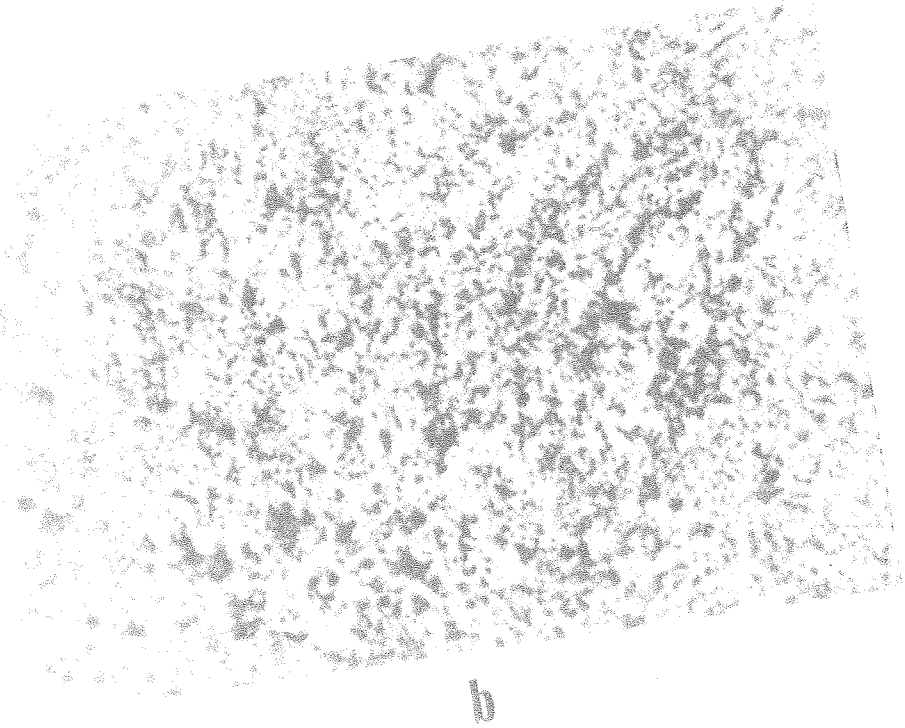

b

X3B769-8586

Fig. 22

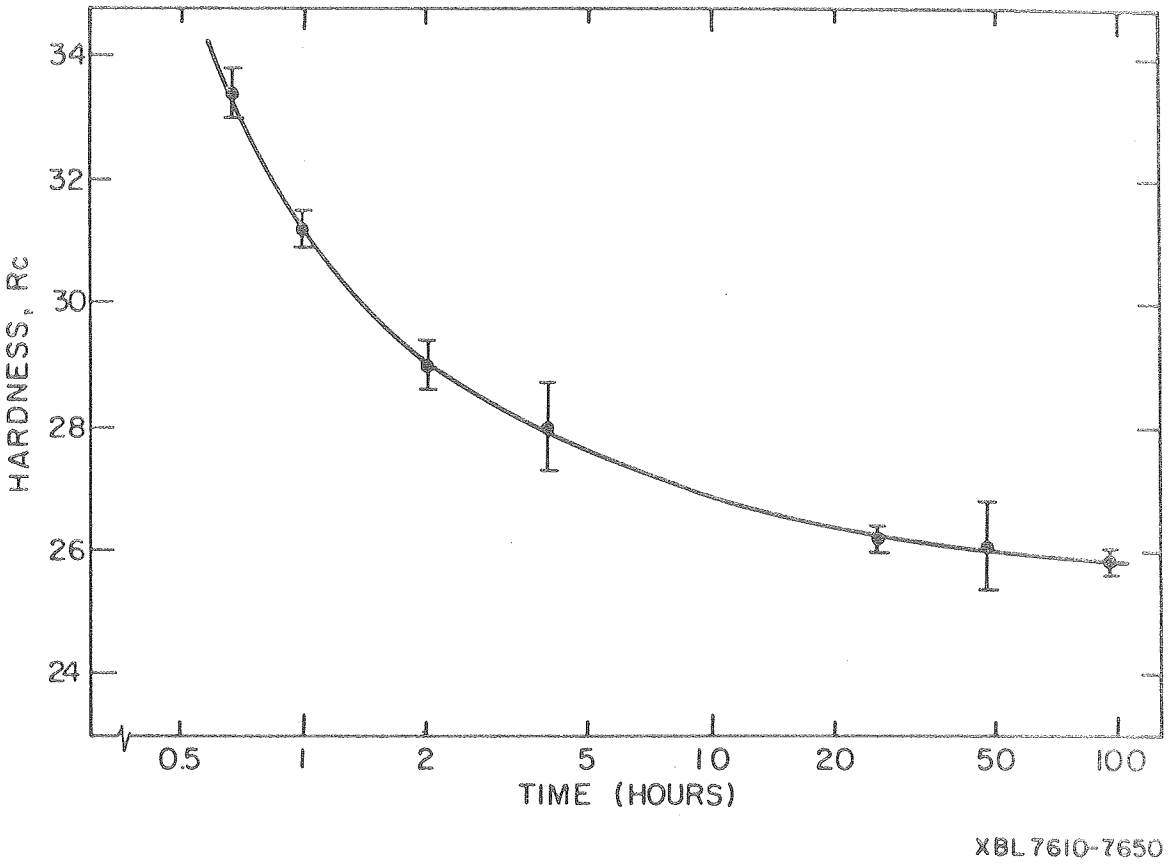

Fig. 23. Age hardening curve (800°C) of the cold-worked Fe-20Mn-2Ti alloy.

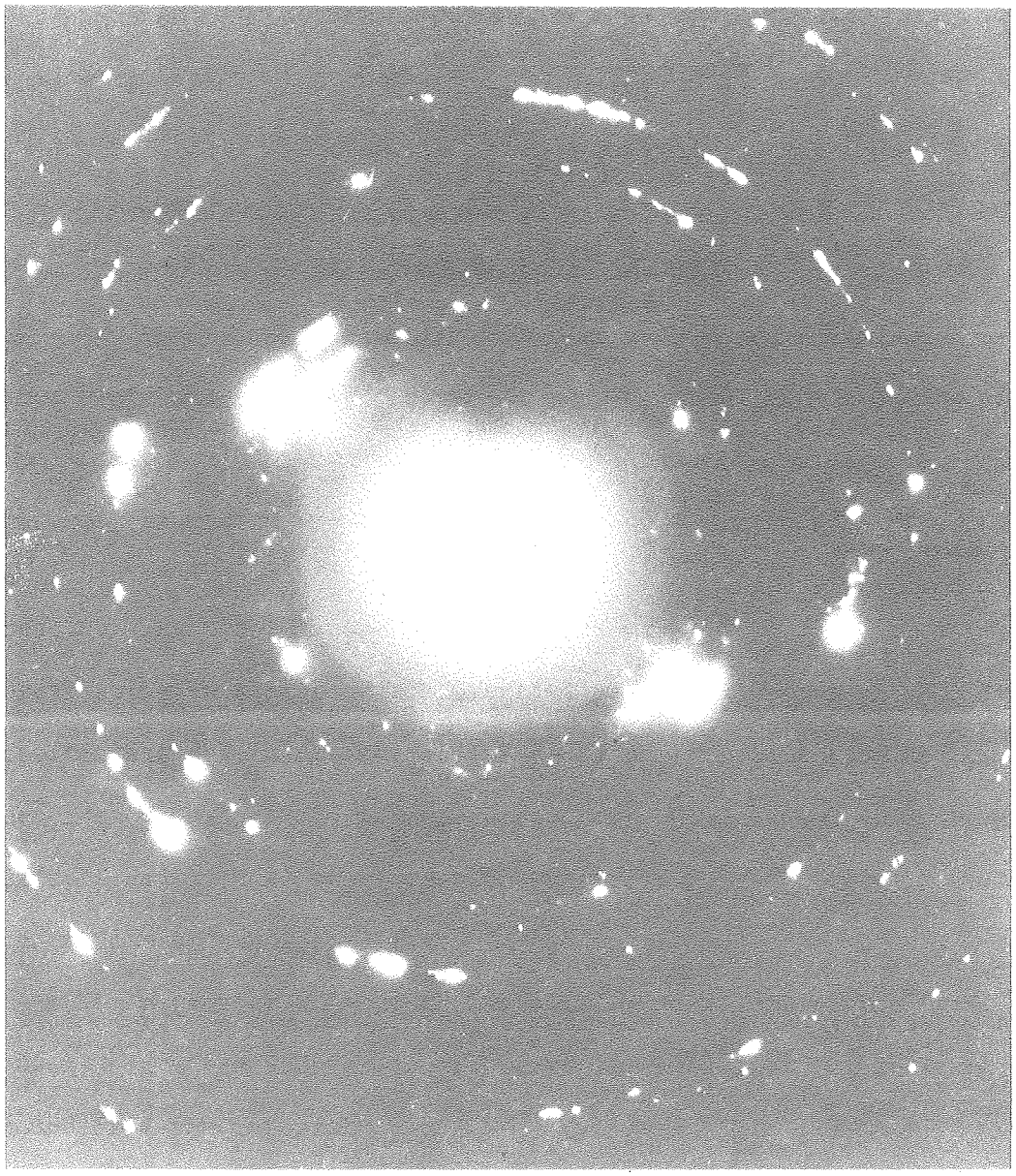

XBB773-1949

Fig. 24

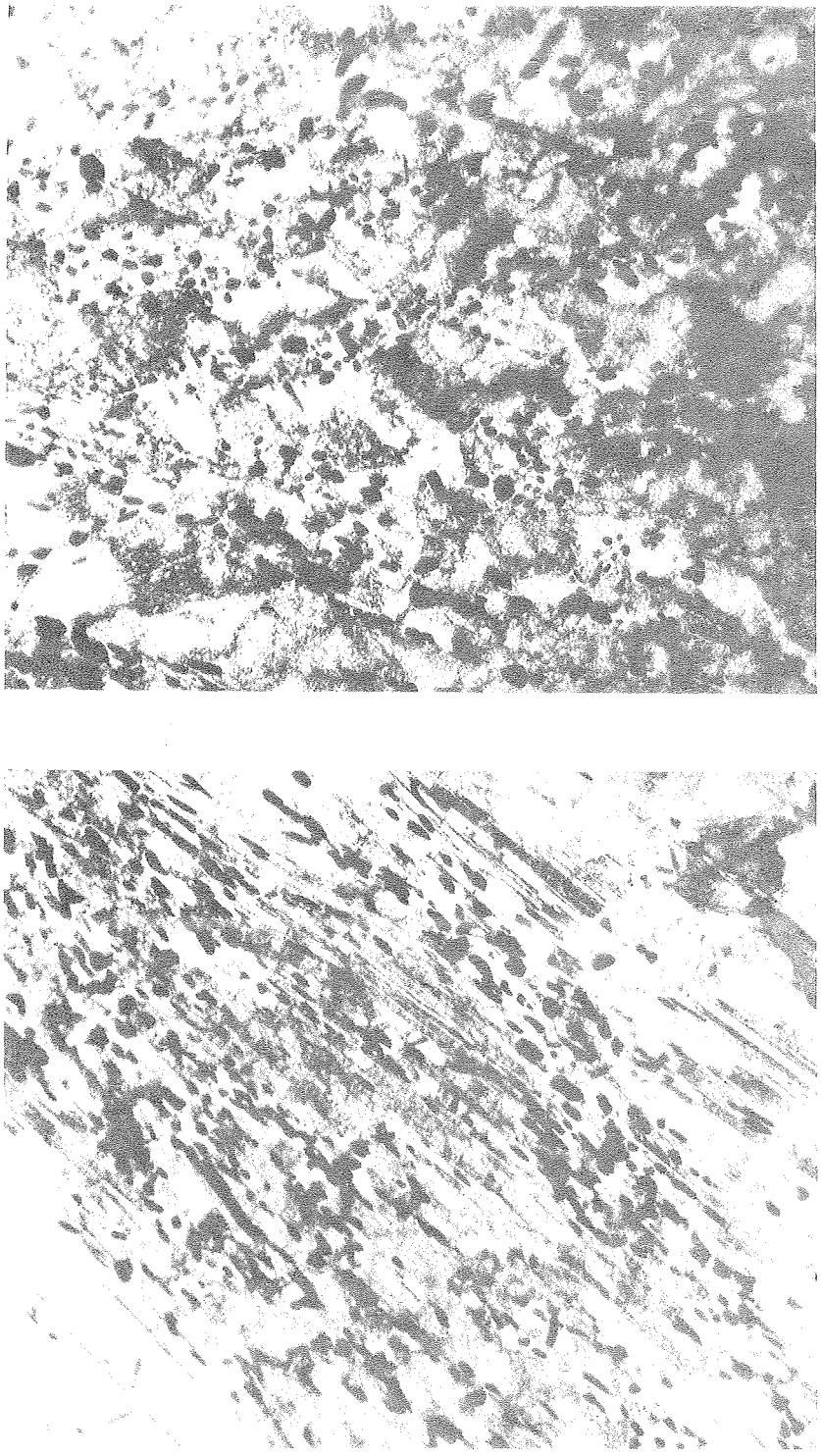

XBB773-1946

Fig. 25

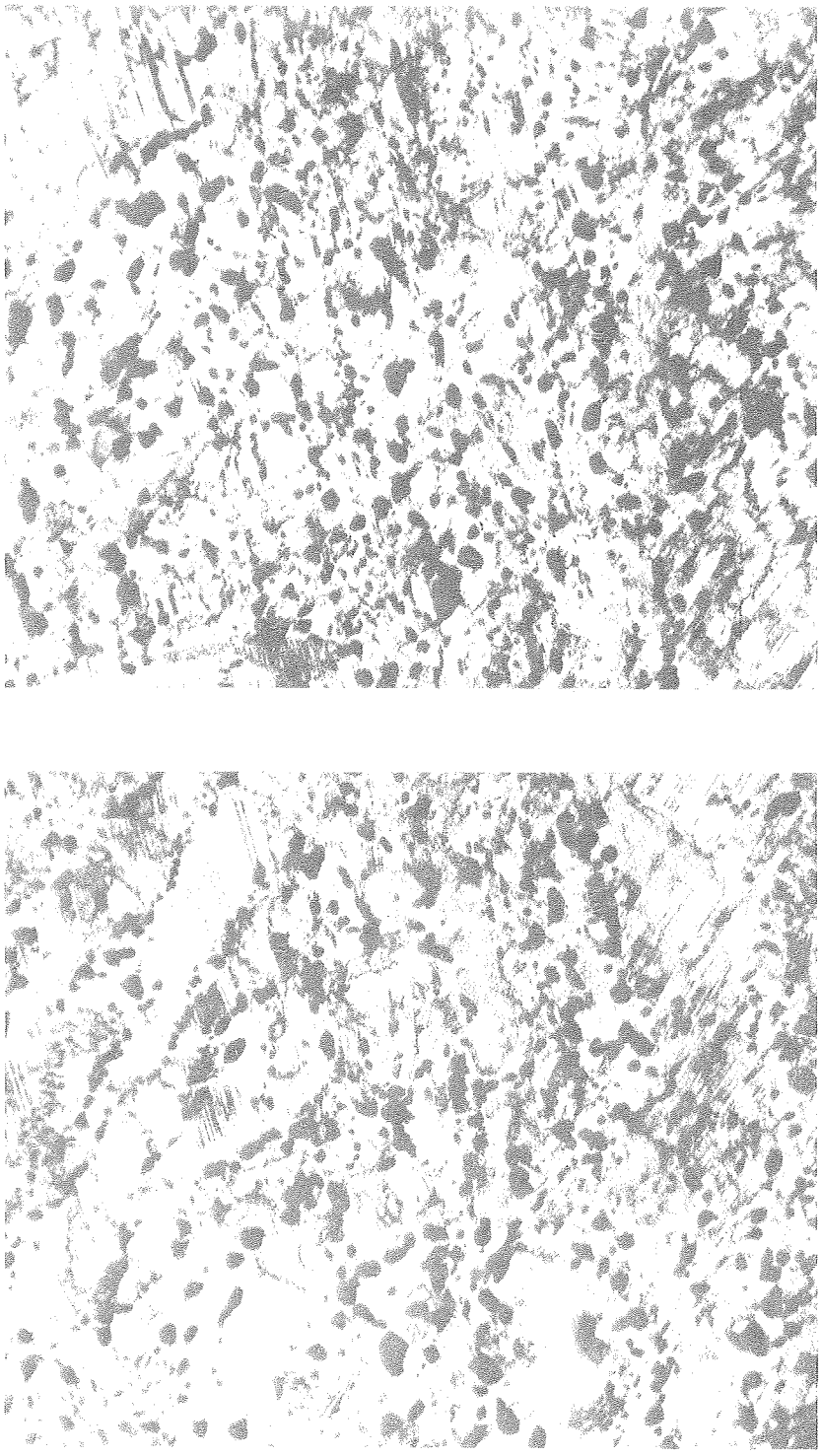

XBB773-1947

Fig. 26

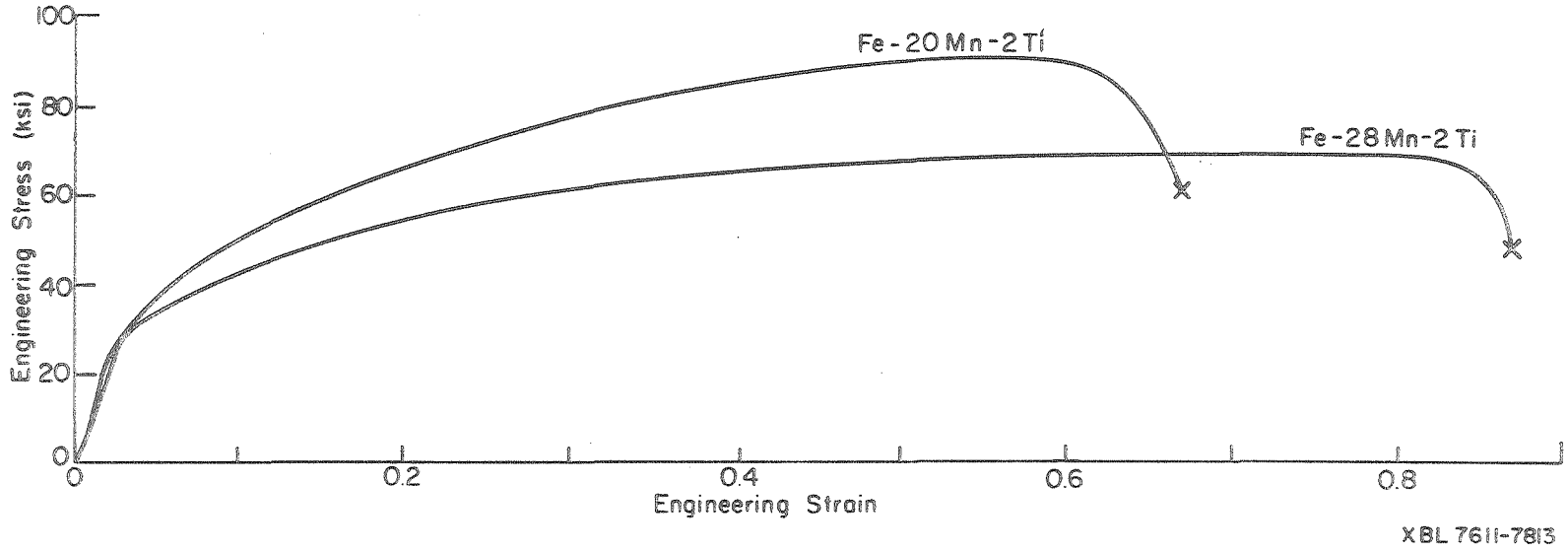

Fig. 27. Engineering stress-strain curves of as-annealed alloys.

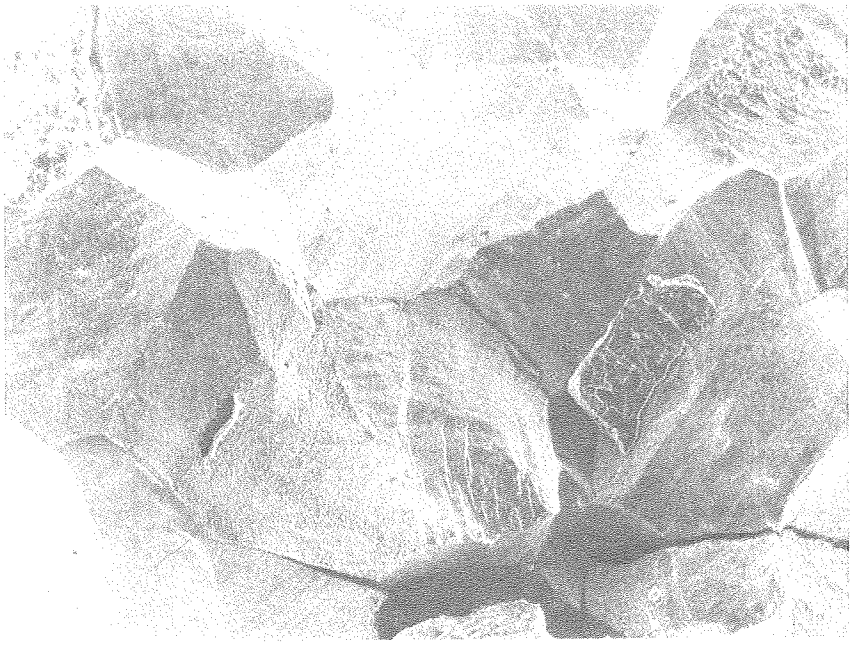

a

b

XBB760-10566

Fig. 28

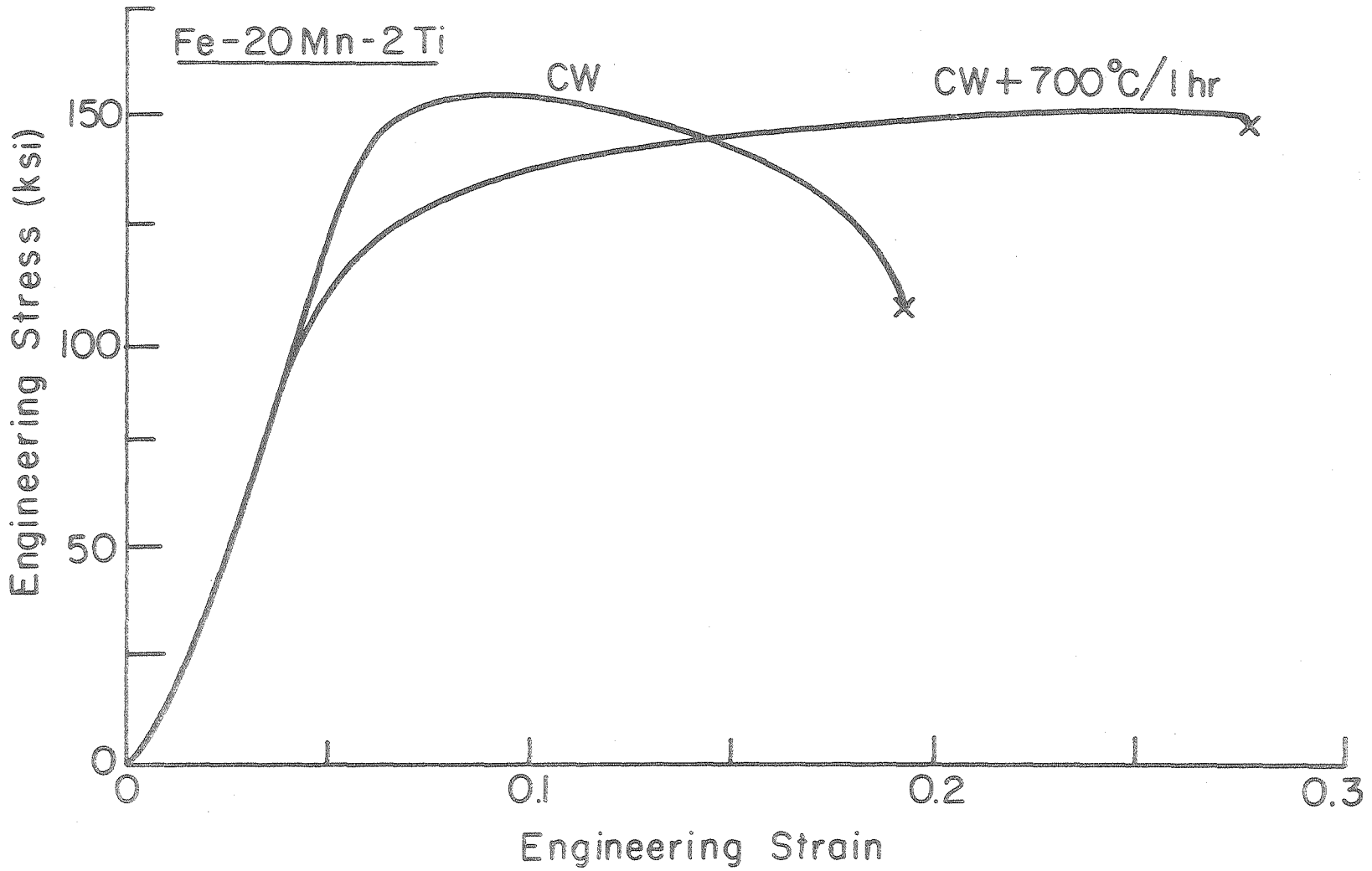

Fig. 29. Engineering strain-stress curves of cold-worked and cold-worked plus aged Fe-20Mn-2Ti alloy.

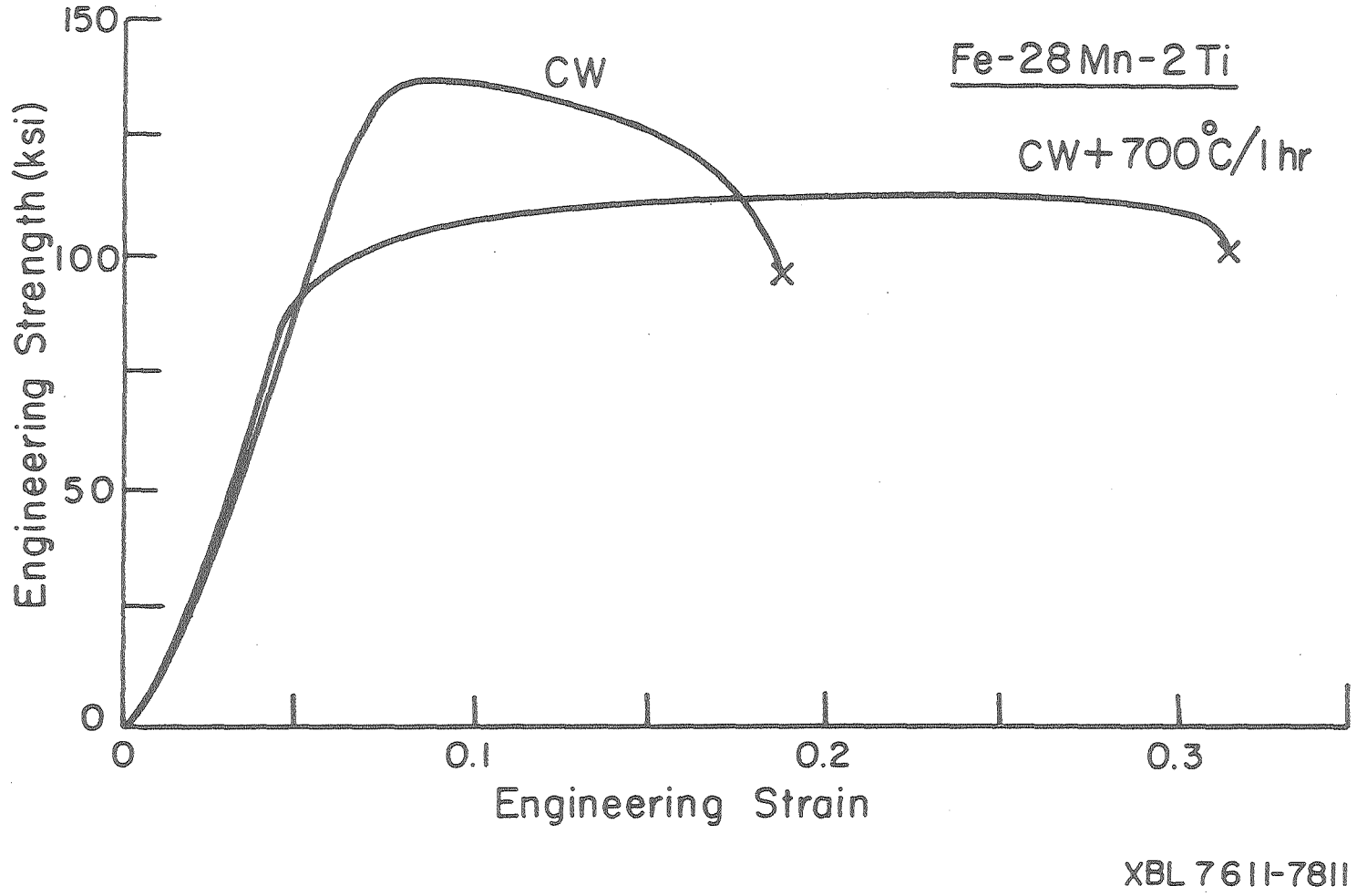

Fig. 30. Engineering strain-stress curves of cold-worked and cold-worked plus aged Fe-28Mn-2Ti alloy.

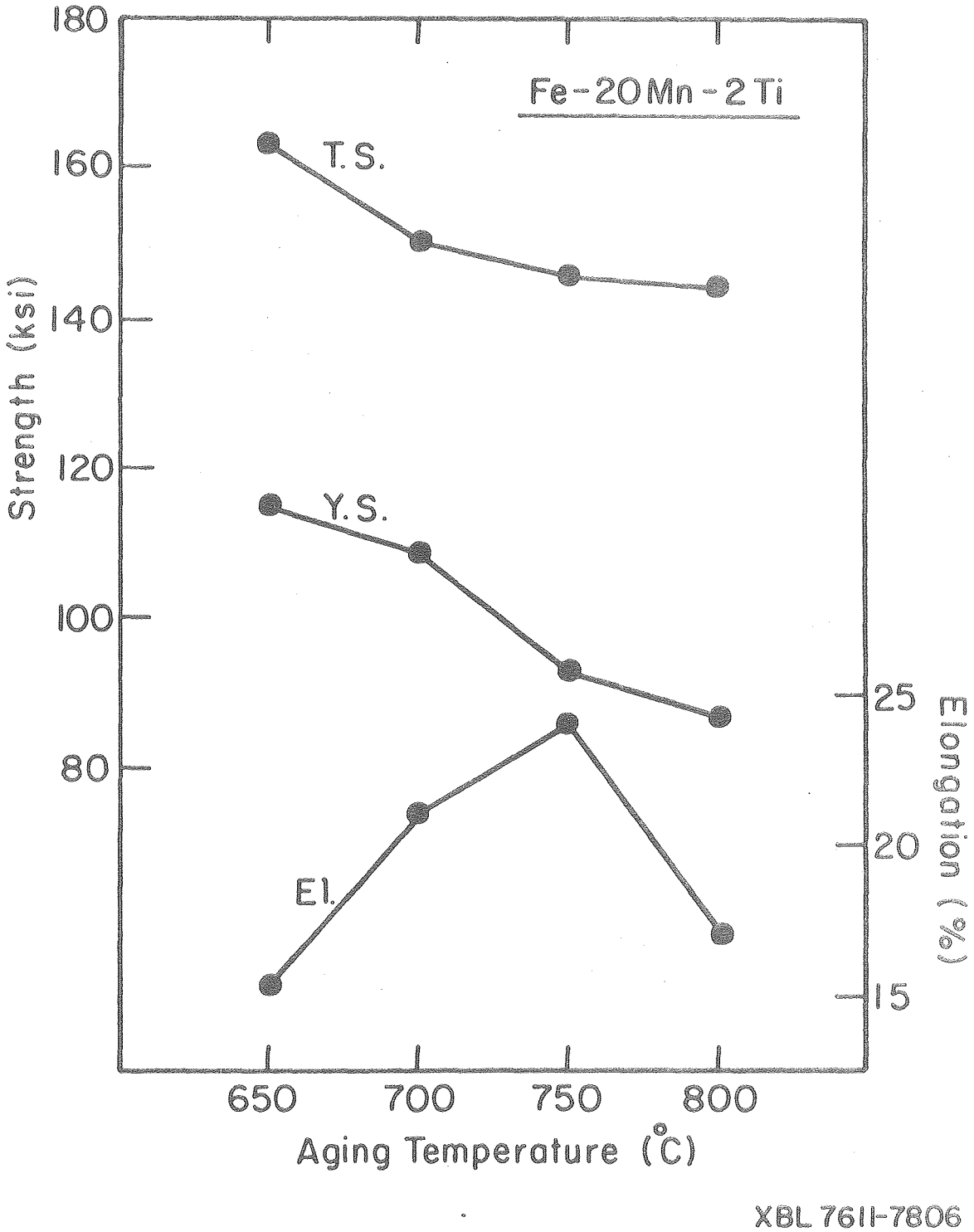

Fig. 31. The effect of aging temperature (1 hr) on the strength and elongation of the cold-worked Fe-20Mn-2Ti alloy.

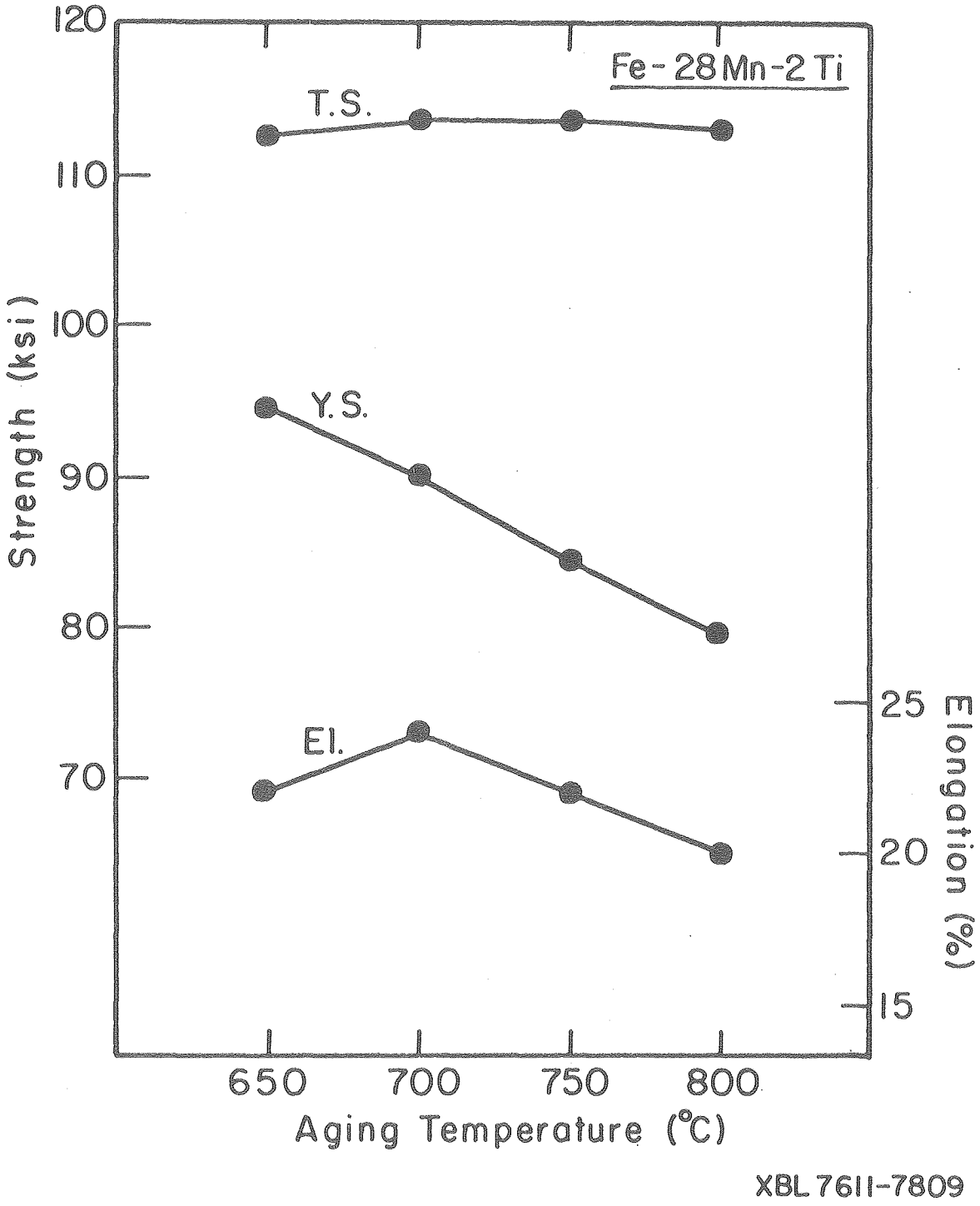

Fig. 32. The effect of aging temperature (1 hr) on the strength and elongation of the cold-worked Fe-28Mn-2Ti alloy.

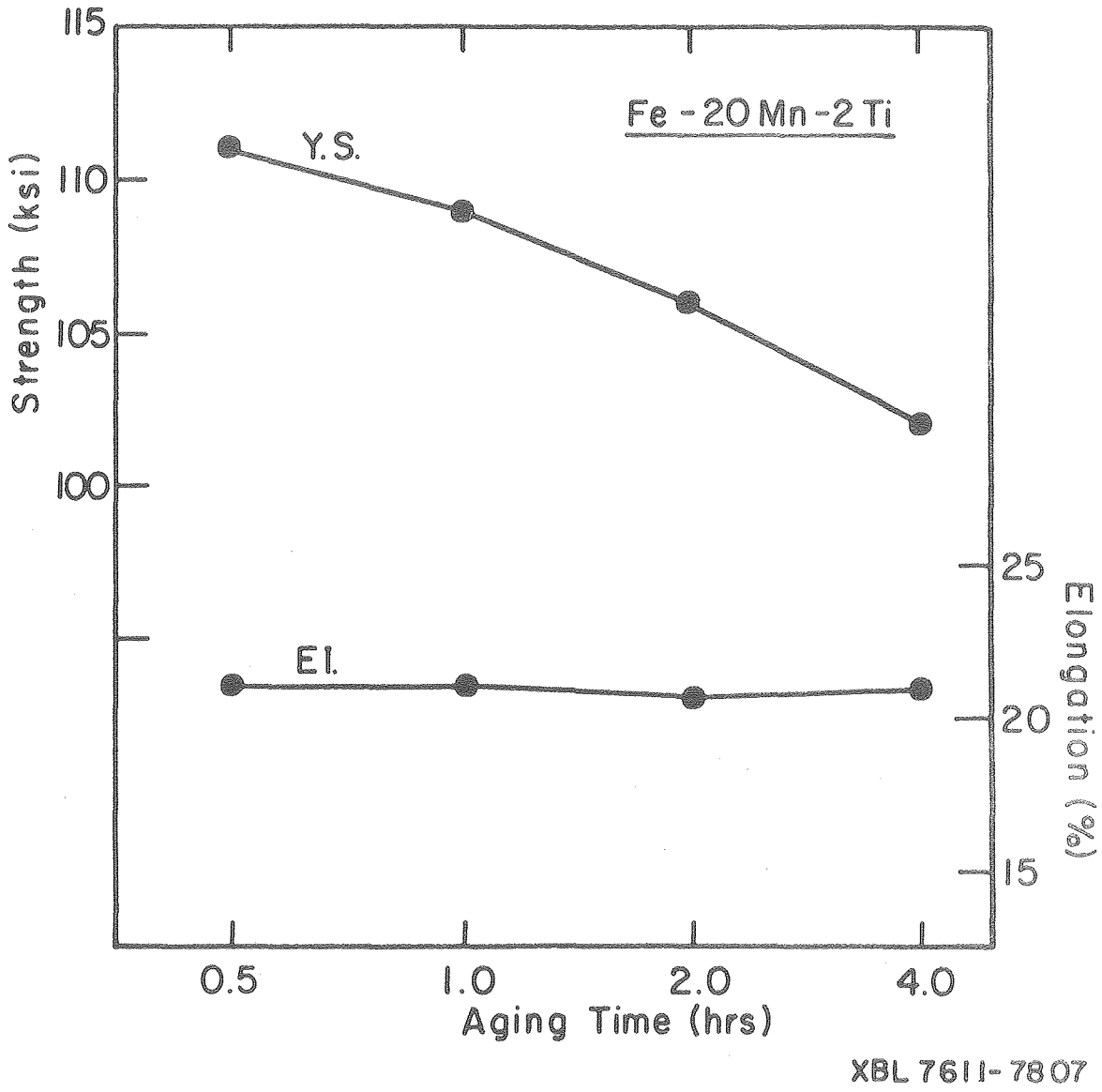

Fig. 33. The effect of aging time (700°C) on the yield strength and elongation of the cold-worked Fe-20Mn-2Ti alloy.

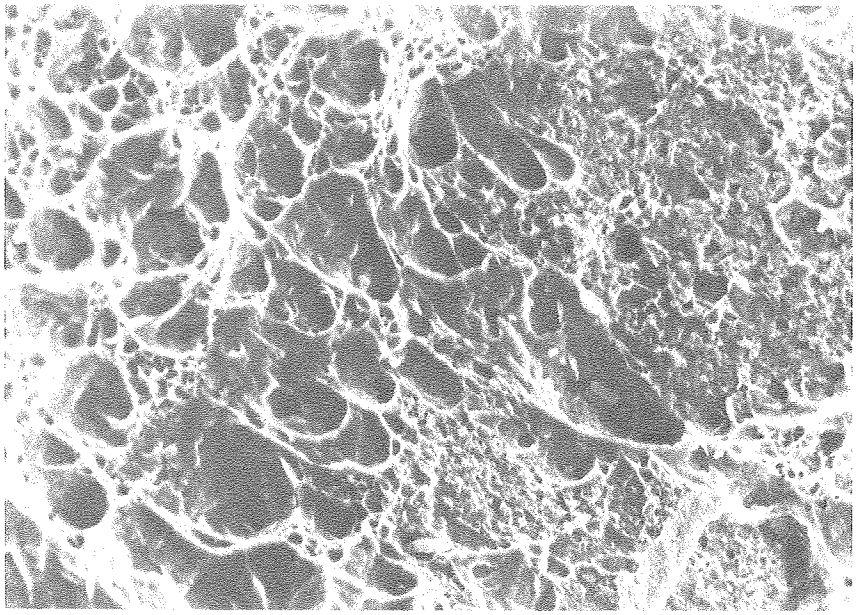

a

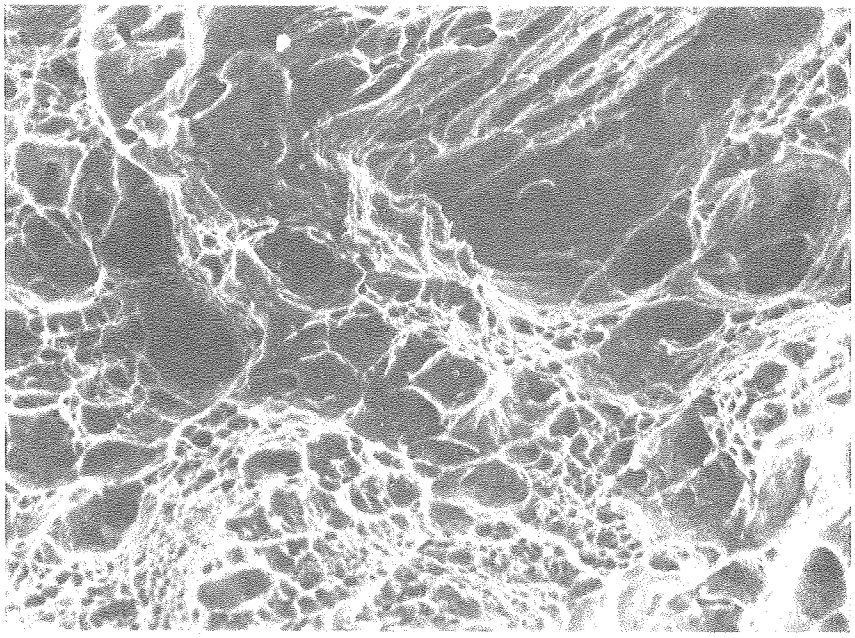

b

XBB760-10427

Fig. 34

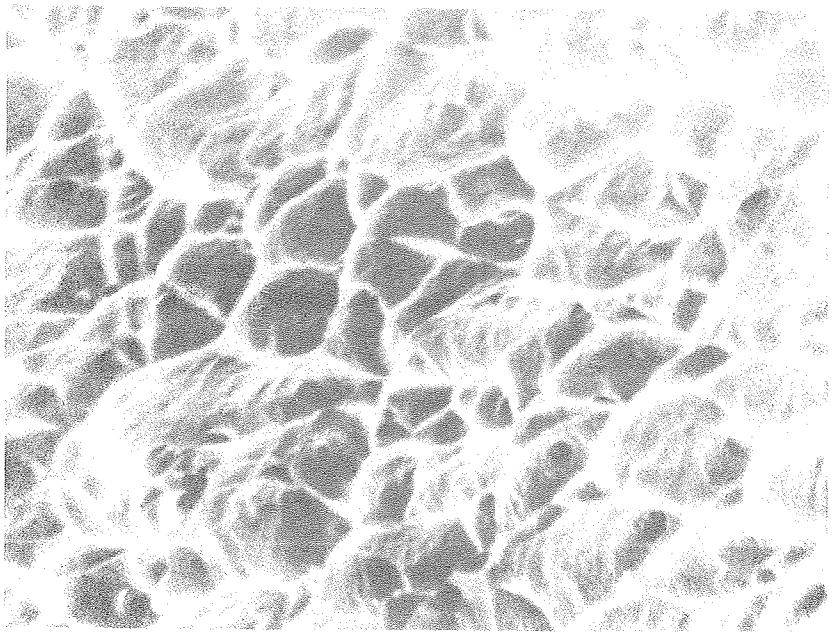

a

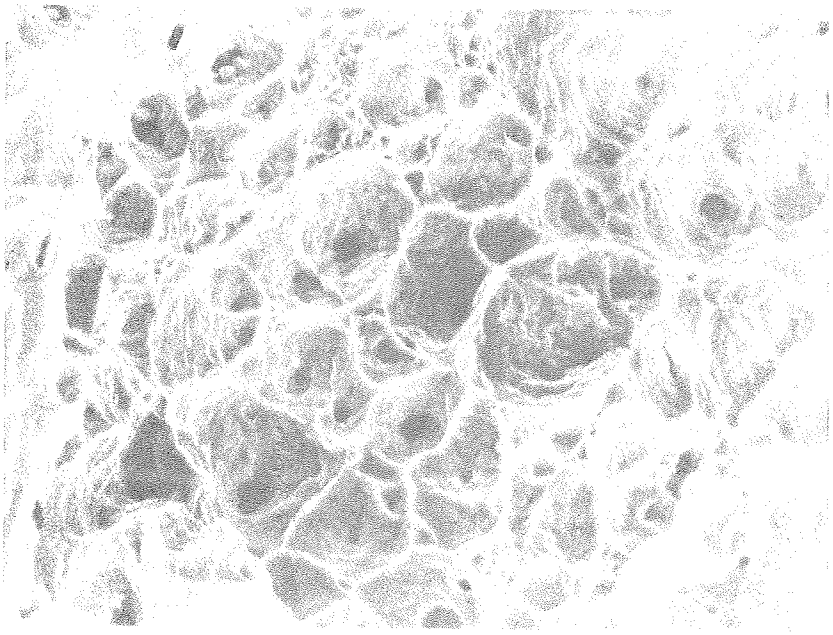

b

XBB760-10567

Fig. 35

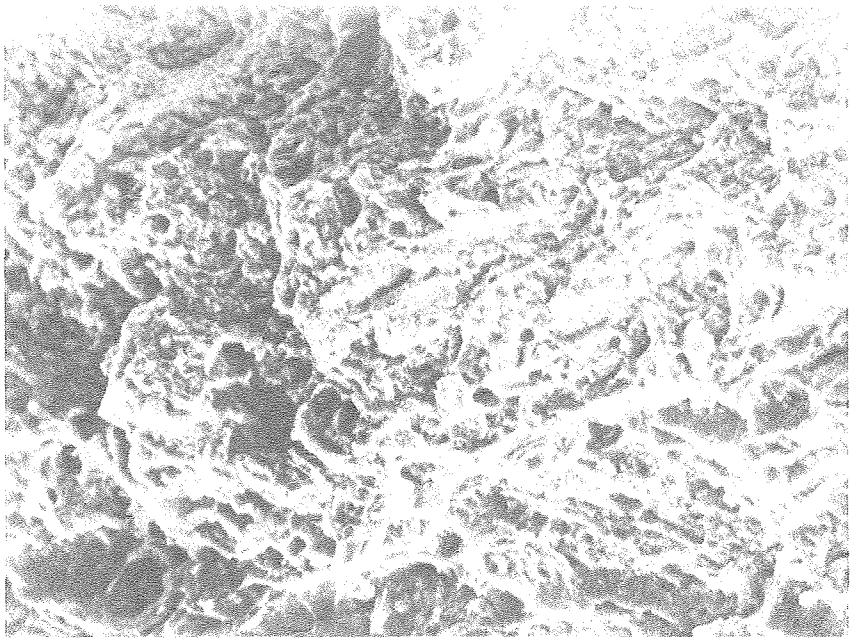

a

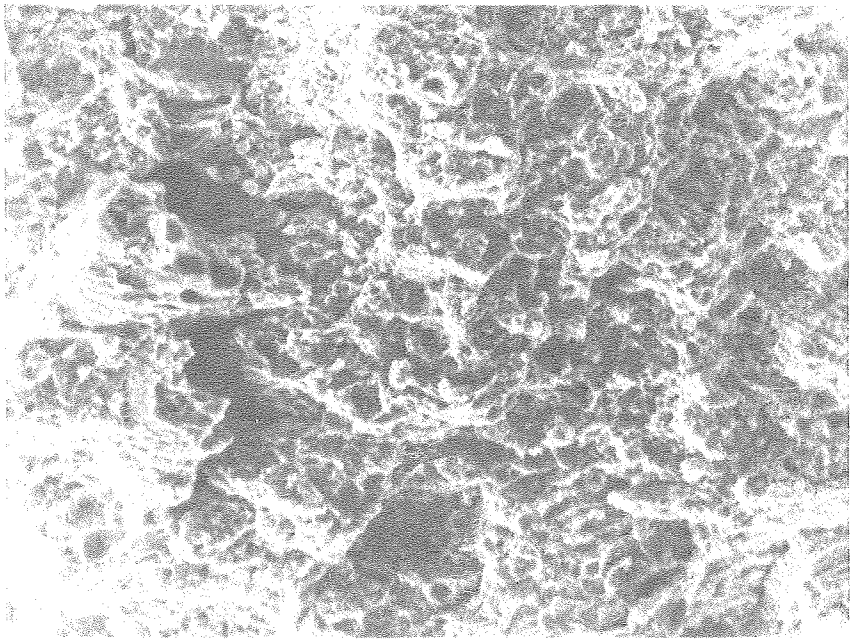

b

XBB760-10426

Fig. 36

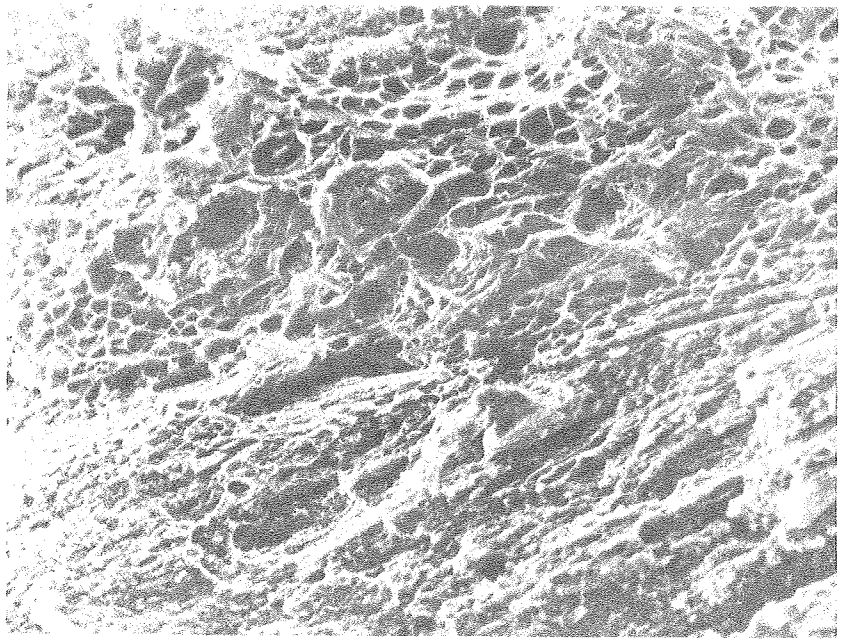

a

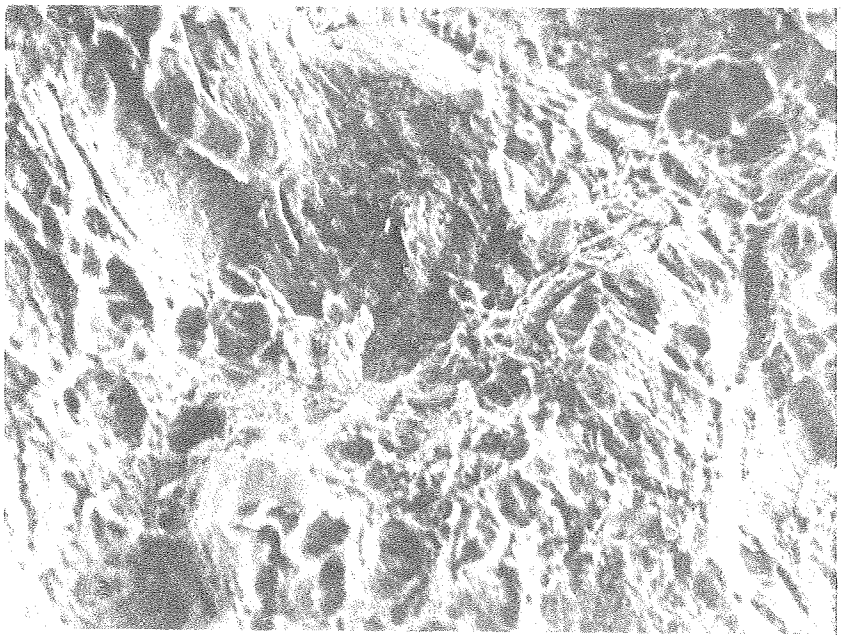

b

XBB760-10565

Fig. 37

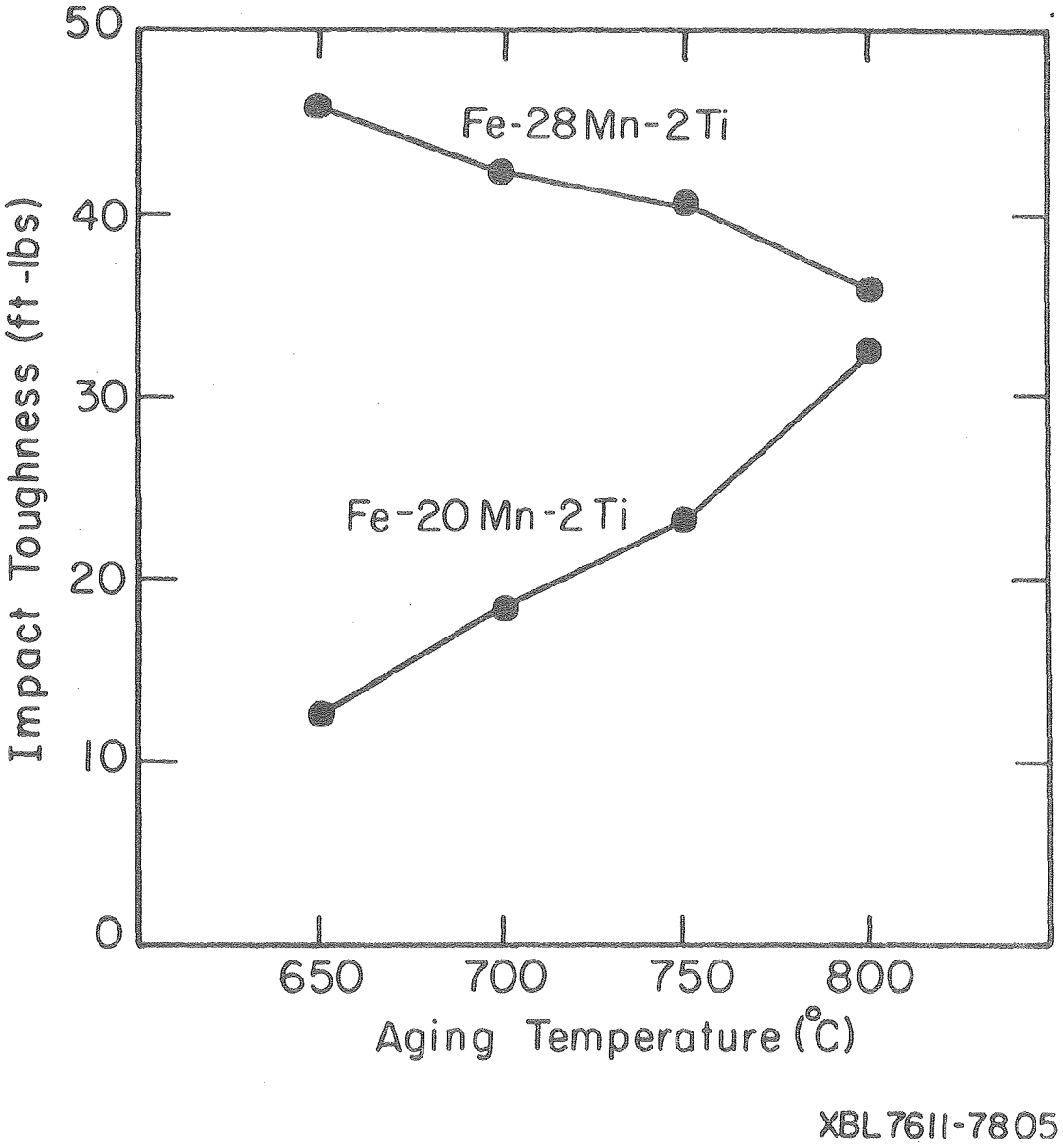

Fig. 38 . The effect of the aging temperature (1 hr) on the Charpy impact energy of the Fe-20Mn-2Ti alloy.

This report was done with support from the United States Energy Research and Development Administration. Any conclusions or opinions expressed in this report represent solely those of the author(s) and not necessarily those of The Regents of the University of California, the Lawrence Berkeley Laboratory or the United States Energy Research and Development Administration.